



Review

# A Review of Transition Metal Nitride-Based Catalysts for Electrochemical Nitrogen Reduction to Ammonia

So Young Park <sup>1</sup>, Youn Jeong Jang <sup>2,\*</sup>  and Duck Hyun Youn <sup>1,\*</sup> 

<sup>1</sup> Department of Chemical Engineering, Department of Integrative Engineering for Hydrogen Safety, Kangwon National University, Chuncheon 24341, Republic of Korea

<sup>2</sup> Department of Chemical Engineering, Hanyang University, Seoul 04763, Republic of Korea

\* Correspondence: yjang53@hanyang.ac.kr (Y.J.J.); youndh@kangwon.ac.kr (D.H.Y.)

**Abstract:** Electrochemical nitrogen reduction (NRR) has attracted much attention as a promising technique to produce ammonia at ambient conditions in an environmentally benign and less energy-consuming manner compared to the current Haber–Bosch process. However, even though much research on the NRR catalysts has been conducted, their low selectivity and reaction rate still hinder the practical application of the NRR process. Among various catalysts, transition metal nitride (TMN)-based catalysts are expected to be promising catalysts for NRR. This is because the NRR process can proceed via the unique Mars–Van Krevelen (MvK) mechanism with a compressed competing hydrogen evolution reaction. However, a controversial issue exists regarding the origin of ammonia produced on TMN-based catalysts. The instability of the TMN-based catalysts can lead to ammonia generation from lattice nitrogen instead of supplied N<sub>2</sub> gas. Thus, this review summarizes the recent progress of TMN-based catalysts for NRR, encompassing the NRR mechanism, synthetic routes, characterizations, and controversial opinions. Furthermore, future perspectives on producing ammonia electrochemically using TMN-based catalysts are provided.

**Keywords:** transition metal nitrides; ammonia; electrochemical nitrogen reduction; catalysts



**Citation:** Park, S.Y.; Jang, Y.J.; Youn, D.H. A Review of Transition Metal Nitride-Based Catalysts for Electrochemical Nitrogen Reduction to Ammonia. *Catalysts* **2023**, *13*, 639. <https://doi.org/10.3390/catal13030639>

Academic Editors: Eun Duck Park, Won Bae Kim and Ji-Wook Jang

Received: 20 February 2023

Revised: 14 March 2023

Accepted: 20 March 2023

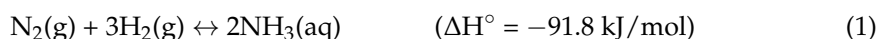
Published: 22 March 2023



**Copyright:** © 2023 by the authors. Licensee MDPI, Basel, Switzerland. This article is an open access article distributed under the terms and conditions of the Creative Commons Attribution (CC BY) license (<https://creativecommons.org/licenses/by/4.0/>).

## 1. Introduction

Next to sulfuric acid, ammonia (NH<sub>3</sub>) is the second most produced chemical in the world and is one of the essential commodities in our lives [1]. NH<sub>3</sub> is employed in various fields, encompassing fertilizers, plastics, textiles, explosives, pharmaceuticals, dyes, and refrigerants [2–4]. In addition, it is considered an attractive hydrogen energy carrier due to its high gravimetric hydrogen density (17.8 wt%) and high volumetric energy density (4.32 kWh/L), similar to methanol [1,4–6]. Furthermore, the liquefaction point of NH<sub>3</sub> (−33.4 °C) is much more favorable for storage and transportation compared to that of hydrogen (−253 °C), facilitating a CO<sub>2</sub>-neutral energy system [7,8].



The Haber–Bosch process (HB process), for which Fritz Haber and Carl Bosch won the Nobel Prize, has been the dominant way to produce industrial ammonia since its invention in 1909 (Equation (1)) [9,10]. Most of the NH<sub>3</sub> produced from this process (over 80%) is converted to fertilizers, enabling the growth of food production and, subsequently, of the world population [10,11]. However, there are several drawbacks to this process. The NH<sub>3</sub> production via the HB process requires high temperatures (400–500 °C) and high pressures (150–300 atm) using Fe-based catalysts [12,13], consuming more than 1% of the total global energy [14]. Additionally, the hydrogen molecules used in the HB process are mainly produced from the steam methane reforming (SMR) of fossil fuels, emitting approximately 1.67 tons of CO<sub>2</sub> per ton of NH<sub>3</sub> [15,16]. Considering that the annual production of NH<sub>3</sub> by the process was 235 million tons in 2021, the amount of CO<sub>2</sub> emission from this process is

equivalent to 390 million tons [1]. Furthermore, due to the energy- and capital-intensive characteristics of the HB process,  $\text{NH}_3$  production sectors are localized in China, Russia, the USA, and India [17]. Thus, an  $\text{NH}_3$  transportation step is required using a ship, tank truck, or pipeline, accompanied by additional cost, energy, and  $\text{CO}_2$  emissions.

Recently, much attention has been paid to electrochemical nitrogen reduction reactions (NRR) to produce ammonia to replace the current HB process. NRR can be carried out at ambient conditions over heterogeneous catalysts with lower energy consumption compared to the HB process. During the NRR process, hydrogen can be obtained from water splitting powered by renewable energy sources such as solar or wind energy. Thus,  $\text{CO}_2$  emissions can be removed at the  $\text{NH}_3$  production step [18–20]. Moreover, NRR enables on-site production of  $\text{NH}_3$  [21,22]; thereby, additional reduction of  $\text{CO}_2$  emissions may be achieved through the reduced need for  $\text{NH}_3$  transportation (Figure 1).

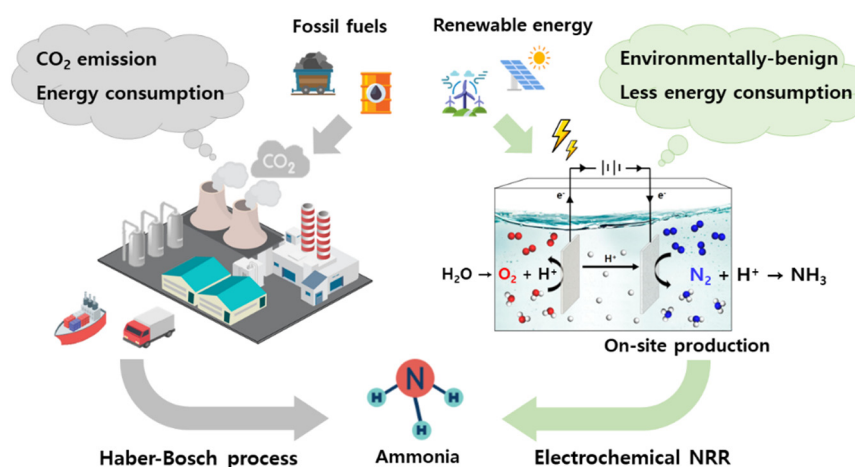


**Figure 1.** Schematic illustration for comparing the HB and NRR processes.

Although the NRR process is environmentally benign with zero carbon emissions and reduced energy consumption, challenging issues, such as insufficient faradaic efficiency (FE) and low  $\text{NH}_3$  yield for practical application, still exist. The FE and  $\text{NH}_3$  yields represent the selectivity for  $\text{NH}_3$  production and the NRR reaction rate (per unit time and unit catalyst mass or unit area), respectively. The equilibrium potential of the hydrogen evolution reaction (HER) is similar to that of NRR. Thus, HER becomes a competing reaction, lowering FE (i.e., selectivity) [23]. Additionally, a large overpotential is required to activate the nitrogen-nitrogen triple bond in an inert  $\text{N}_2$  molecule, resulting in a low  $\text{NH}_3$  yield (i.e., reaction rate). Until now, various catalysts, including precious metal-based materials [24–32], transition metal compounds (transition metal carbide [33–35]/nitride [36–38]/sulfide [39–41]/oxide [42–44]/phosphide [45–47]), and non-metallic series [48–50], have been employed for NRR to improve the FE and  $\text{NH}_3$  yields. Despite many efforts, the NRR performances of the reported catalysts are still far below practical utilization goals (current density of  $300 \text{ mA cm}^{-2}$ , FE of 90%, and energy efficiency of 60%) according to the REFUEL program of the US Department of Energy [51]. Thus, the investigation of highly active, durable, and cost-effective catalysts for NRR is strongly required.

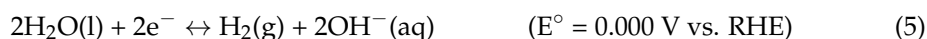
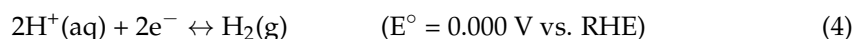
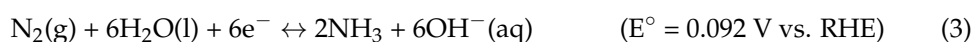
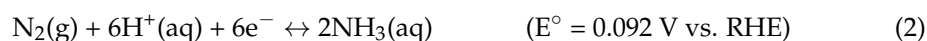
Currently, transition metal nitride (TMN)-based catalysts are extensively studied as a new class of non-precious metal catalysts for NRR. TMN is an interstitial alloy that incorporates nitrogen atoms into the interstitial sites of the crystal lattice of metals [52]. TMN has unique physical properties, including hardness, wear resistance, and superconductivity, which renders them suitable for use as coating agents for cutting tools and refractory materials [53–55]. More importantly, TMN has been employed as a catalyst in various traditional catalytic reactions to replace Pt-group metals, including hydrogenation and hydrodesulfurization, because they exhibit similar electronic structures to those of noble metals [55–57]. Additionally, TMNs have gained great attention in the field of energy, such

as fuel cells [58,59], photocatalysts [60,61], solar cells [62,63], and water splitting [64,65]. Especially in NRR, many TMN-based catalysts have been reported as potential catalysts inspired by density functional theory (DFT) results [66–69]. The most promising candidates turned out to be VN, CrN, NbN, and ZrN because they might be more selective toward NRR than the competing HER [70].

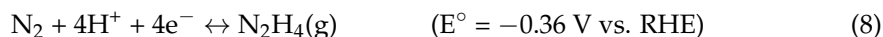
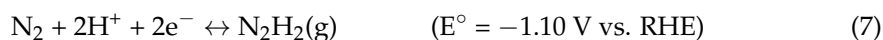
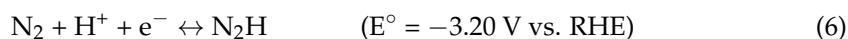
In this review, we present an overview of the state-of-the-art TMN-based catalysts for NRR, focusing on the reaction mechanism (such as the Mars–Van Krevelen mechanism), synthetic routes, and characterization methods. In addition, conflicting opinions pointing out the inability of TMN to contribute to NRR due to their instability will also be considered. Finally, challenges and future perspectives will be discussed.

## 2. Mechanisms of NRR

The following equations represent the reactions for NRR in acidic (Equation (2)) and basic solutions (Equation (3)), with the equilibrium potentials referenced to the reversible hydrogen electrode (RHE). Equations (4) and (5) are for HER under acidic and alkaline media, respectively. The NRR involves six electrons and is thus kinetically unfavorable compared to the two-electron-involved HER. In addition, the equilibrium potentials of NRR are similar to those of HER in both acidic and alkaline conditions, suggesting that HER is a competitive reaction to NRR.



Consisting of multiple protonation steps, NRR generates several intermediates during the process, which may act as a blockage, making it difficult to react thermodynamically. The initial addition of the proton and electron to  $\text{N}_2$  needs a highly negative equilibrium potential (i.e., a very high energy barrier), revealing that the formation of  $\text{N}_2\text{H}$  is difficult (Equation (6)). Furthermore, the  $\text{N}_2\text{H}$  can be further reduced to two possible intermediates, diazene ( $\text{N}_2\text{H}_2$ ) and hydrazine ( $\text{N}_2\text{H}_4$ ). The equilibrium potentials for diazene and hydrazine (Equations (7) and (8)) are larger compared to  $\text{NH}_3$  production (Equations (2) and (3)), indicating a thermodynamic difficulty in the electroreduction of  $\text{N}_2$ .



In general, mechanisms of NRR are classified as the dissociative pathway, the associative pathway, and the Mars–Van Krevelen (MvK) pathway (Figure 2). In the dissociative pathway (Figure 2a), by breaking the  $\text{N}\equiv\text{N}$  bond, two N atoms are first adsorbed solely on the catalyst surface, and subsequent hydrogenation occurs to produce  $\text{NH}_3$ . The cleavage of the triple bond of  $\text{N}_2$  requires a large quantity of energy (945 kJ/mol) [71,72]. Given that the HB process follows this pathway, it is not surprising that the HB process needs such a high temperature, high pressure, and substantial energies. In the associative pathway,  $\text{N}_2$  molecules are first adsorbed on the catalyst surface without the  $\text{N}\equiv\text{N}$  bond breaking, followed by the addition of hydrogen atoms. Thus, the  $\text{N}\text{--}\text{N}$  bond is broken simultaneously with the generation of the first  $\text{NH}_3$  molecule. This mechanism can be subclassified as the distal pathway, the alternative pathway, and the enzymatic pathway. In the associative distal pathway (Figure 2b), the  $\text{N}_2$  molecule reaches the catalyst surface and is adsorbed in end-on mode. The remote N atom (i.e., the distal N atom) is hydrogenated first and released as  $\text{NH}_3$ . Another N atom remaining on the catalyst surface is continuously reduced to pro-

duce the second  $\text{NH}_3$ . In the associative alternative pathway (Figure 2c), which is different from the distal pathway, the H atoms are added to both N atoms, and two molecules of  $\text{NH}_3$  are released consecutively. In the enzymatic pathway (Figure 2d), the two N atoms of the  $\text{N}_2$  molecule are both adsorbed on the surface of the catalyst (side-on mode). Then two N atoms are reduced by H atoms alternatively, as demonstrated for the associative alternative pathway.

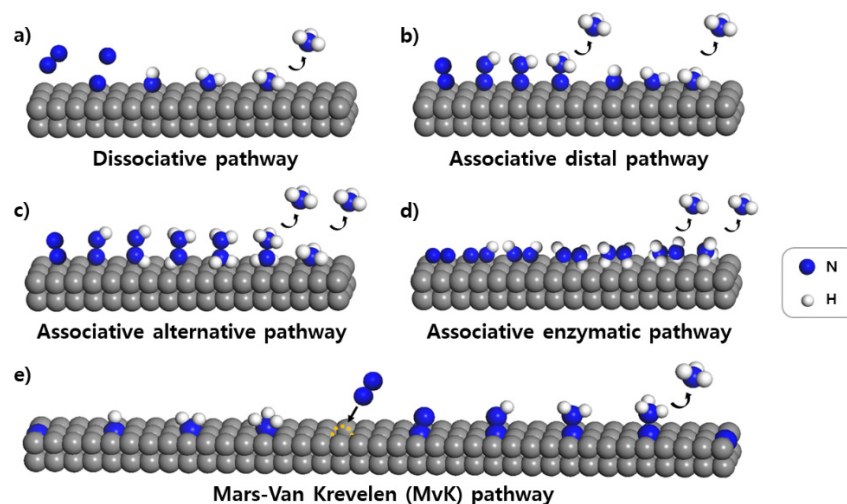


**Figure 2.** The mechanisms of NRR. (a) Dissociative pathway; (b) associative distal pathway; (c) associative alternative pathway; (d) associative enzymatic pathway; and (e) Mars–Van Krevelen (MvK) pathway.

The MvK mechanism has been suggested to explain the NRR mechanism for the TMN catalysts (Figure 2e) and is in contrast to the other mechanisms. Firstly, H atoms are attached to the surface N atom of the TMNs. The N atom is electrochemically reduced, and the first  $\text{NH}_3$  is released, leaving an N vacancy on the catalyst surface. Secondly, the N-vacancies are replenished by the supplied  $\text{N}_2$  molecules, and a subsequent hydrogenation process occurs, producing the second  $\text{NH}_3$ . Finally, the catalyst's surface is regenerated, and this cycle is repeated during the NRR. Notably, the MvK mechanism possesses unique merits. The first  $\text{NH}_3$  production does not require the adsorption and cleavage of  $\text{N}_2$  on the surface of the catalyst, reducing the energy barrier for  $\text{NH}_3$  production. Furthermore, the surface energy of the catalysts with N-vacancies is higher, facilitating favorable adsorption of  $\text{N}_2$  and cleavage of the  $\text{N}\equiv\text{N}$  bond. For the TMN catalyst, Abghoui et al. calculated the important factors in each step, such as the initial  $\text{NH}_3$  formation, N-vacancy replenishment, catalytic cycle endurance, stability of the N vacancies, and poisoning. They claimed that the most promising catalysts were VN, CrN, ZrN, and NbN, and their rocksalt (100) facet was the most likely to be active among the various facets [70]. Because candidates have stable N vacancies and surface vacancies free from poisoning by  $-\text{H}$  or  $-\text{O}$ , higher NRR activities than those of HER can be expected.

### 3. TMN-Based Catalysts

#### 3.1. TMN-Based Catalysts with Catalytic Activity

##### 3.1.1. Vanadium Nitride-Based Catalysts

VN nanowire array on carbon cloth (VN/CC) was synthesized by annealing  $\text{V}_2\text{O}_5$  precursor under  $\text{NH}_3$  flow and utilized as a catalyst for NRR [73]. The nanowire structure can be confirmed through scanning electron microscope (SEM) images (Figure 3a). The VN/CC showed an FE of 3.58% with an  $\text{NH}_3$  yield of  $2.48 \times 10^{-10} \text{ mol s}^{-1} \text{ cm}^{-2}$  at  $-0.3 \text{ V}$  vs. RHE in a 0.1 M HCl solution. At potentials lower than  $-0.3 \text{ V}$ , the FE and  $\text{NH}_3$  yields decreased remarkably because HER became the dominant reaction. Additionally, no hydrazine was detected through the Watt and Chrisp method, which indicates a great

selectivity of the VN/CC. The FE and NH<sub>3</sub> yields were maintained without significant performance decay over 10 times of consecutive recycling tests at −0.3 V. The stability test showed no significant changes in the catalysts' morphology, crystallinity, or surface states, suggesting the activity and stability of the VN/CC for NRR in acidic media.

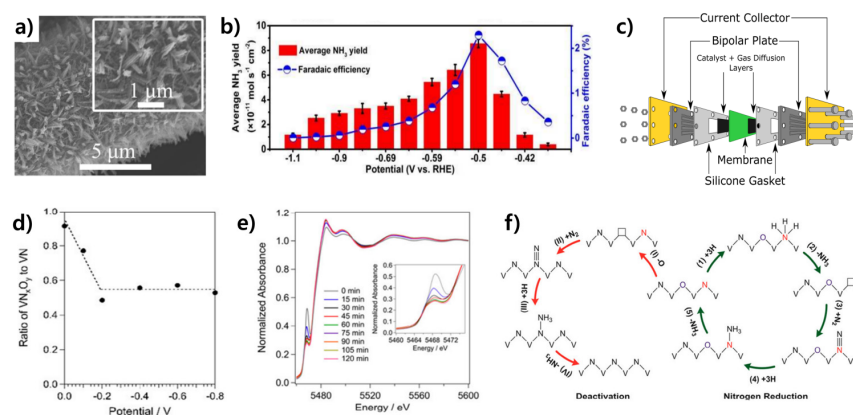


**Figure 3.** (a) SEM image of VN/CC. (b) NH<sub>3</sub> yield and FE at different potentials on VN/TM. (c) Schematic illustration of MEA. (d) VN<sub>x</sub>O<sub>y</sub>/VN ratio after 1 h of reaction at various potentials. (e) Operando XAS results of K-edge XANES of VN at −0.2 V. (f) Proposed MvK mechanism of NRR and deactivation pathway on VN<sub>0.7</sub>O<sub>0.45</sub>. Reproduced with permission from the Royal Society of Chemistry [73] and the American Chemical Society [37,74,75].

A VN nanosheet on Ti mesh (VN/TM) was fabricated through the nitridation of a VO<sub>2</sub> nanosheet array on Ti mesh (VO<sub>2</sub>/TM) under NH<sub>3</sub> flow for 3 h at 700 °C [74]. The SEM and transmission electron microscope (TEM) showed that the catalyst is composed of VN nanosheets, and the energy dispersive X-ray spectroscopy (EDX) mapping results confirmed the uniform distribution of the V and N elements on Ti. In the linear sweep voltammetry (LSV) results, the current density under N<sub>2</sub> flow was higher than that under Ar flow, suggesting that VN/TM is active for NRR in 0.1 M HCl. It achieved an NH<sub>3</sub> yield of  $8.40 \times 10^{-11} \text{ mol s}^{-1} \text{ cm}^{-2}$  at −0.5 V with an FE of 2.25% (Figure 3b). The TM itself did not show NRR activity, further suggesting that VN is an active site in VN/TM. In the EDX results after the NRR test under Ar flow for 3 h, the N in VN disappeared, indicating the MvK mechanism of VN/TM. In the NMR spectra using the <sup>15</sup>N<sub>2</sub> isotope, both doublet peaks of <sup>15</sup>NH<sub>4</sub><sup>+</sup> and triplet peaks of <sup>14</sup>NH<sub>4</sub><sup>+</sup> were detected, further implying that the NRR proceeded through the MvK mechanism on VN/TM. In addition, FE and NH<sub>3</sub> yield values were maintained for 10 recycling tests, indicative of good stability of VN/TM toward NRR.

Yang et al. employed a membrane electrode assembly (MEA) configuration to study the NRR for VN nanoparticles due to the low solubility of N<sub>2</sub> in an aqueous solution (Figure 3c) [37]. The VN and Pt/C catalysts were loaded on carbon paper and used as cathodes and anodes, respectively. In this setup, the Pt anode acted as a reversible hydrogen electrode. At −0.1 V, the VN catalyst exhibited an FE of 6.0% with an NH<sub>3</sub> yield of  $3.3 \times 10^{-10} \text{ mol s}^{-1} \text{ cm}^{-2}$ . A steady-state NH<sub>3</sub> yield of  $1.1 \times 10^{-10} \text{ mol s}^{-1} \text{ cm}^{-2}$  and a 1.6% FE were maintained for 116 h. In contrast, at −0.2 V, an FE of 6.5% and an NH<sub>3</sub> yield of  $5.0 \times 10^{-10} \text{ mol s}^{-1} \text{ cm}^{-2}$  were recorded within the first hour. However, the NH<sub>3</sub> yield at −0.2 V plunged more than 95% to  $1.1 \times 10^{-11} \text{ mol s}^{-1} \text{ cm}^{-2}$  after 2 h. NRR tests with a <sup>15</sup>N<sub>2</sub> isotope proved that the reaction was conducted via the MvK mechanism. Triplet (<sup>14</sup>NH<sub>4</sub><sup>+</sup>) and doublet (<sup>15</sup>NH<sub>4</sub><sup>+</sup>) peaks were detected. The active phase and deactivation mechanism were identified by characterizing fresh and spent VN samples. VN<sub>0.7</sub>O<sub>0.45</sub> is proposed as an active phase from the X-ray photoelectron spectroscopy (XPS) results because the VN<sub>0.7</sub>O<sub>0.45</sub>/VN ratios correlate well with the reactivity results (Figure 3d). Furthermore, in the operando X-ray absorption near edge structure (XANES) of the V K-edge results, the intensity of the pre-edge peak at 5468.4 eV (oxynitride species) decreased with increasing NRR reaction time, and more negative potentials accelerated the intensity decreasing rate

(Figure 3e). These results indicate that the conversion of  $\text{VN}_{0.7}\text{O}_{0.45}$  to VN causes the deactivation of NRR. The deactivation mechanism was hypothesized such that since the active phase,  $\text{VN}_{0.7}\text{O}_{0.45}$ , is unstable under reduction conditions, O atoms nearby N atoms are removed faster at a more negative potential. Hence, the generated vacancies are filled with  $\text{N}_2$ , finally producing the inactive phase VN (Figure 3f).

### 3.1.2. Chromium Nitride-Based Catalysts

For the  $\text{Cr}_2\text{N}$  and CrN catalysts, the active species and deactivation pathway were investigated using an MEA configuration, as shown in Figure 3c [75]. The commercial  $\text{Cr}_2\text{N}$  (CN-P) and CrN (CN-S) synthesized by the urea-glass route have been used for NRR. The CN-P showed an  $\text{NH}_3$  yield of  $1.4 \times 10^{-11} \text{ mol s}^{-1} \text{ cm}^{-2}$  and an FE of 0.58% at  $-0.2 \text{ V}$  for 24 h under  $80^\circ\text{C}$  conditions. From  $-0.2 \text{ V}$  to  $-0.8 \text{ V}$ , the  $\text{NH}_3$  yield increased, but the FE decreased because HER became the dominant reaction as the potential increased. Additionally, the catalyst deactivation of the CN-P is more severe at a more negative potential. Over 24 h, the  $\text{NH}_3$  yield decreased by 20% at  $-0.2 \text{ V}$ , while an 87% decrease at  $-0.8 \text{ V}$  was observed. In the NMR spectra using the  $^{15}\text{N}_2$  isotope, both  $^{15}\text{NH}_4^+$  and  $^{14}\text{NH}_4^+$  peaks were detected, confirming the MvK mechanism on the CN-P catalyst. The N/Cr ratio measured from the XPS results was pointed out as an important parameter. After the reaction at  $-0.2$  and  $-0.4 \text{ V}$ , the N/Cr ratio was around 0.5, similar to the fresh sample ratio. However, the ratio abruptly decreased after operation at  $-0.6$  and  $-0.8 \text{ V}$ . Especially at  $-0.8 \text{ V}$ , as observed by depth-profiling XPS, the N/Cr ratio was 0.2 (Figure 4a). These results indicate that N was leached out on the catalyst surface during NRR, which in turn caused the deactivation of CN-P. The NRR performance of CN-S was compared with CN-P. The FE and  $\text{NH}_3$  yields of CN-S were 4 and 5 orders of magnitude times lower than those of CN-P. According to XPS analysis, all species in CN-P were present except for the  $\text{Cr}_2\text{N}$ , which provides strong evidence that  $\text{Cr}_2\text{N}$  is the active phase for NRR.

Ma et al. reported that CrN is an active catalyst for NRR [38]. Here, CrN was synthesized by a glucose-mediated hydrothermal calcination route and ammonolysis. Glucose is used for creating a hollow structure of metal oxide, which results from the collapse of the carbon body during calcination. A metal precursor prepared by hydrothermal treatment was converted to  $\text{Cr}_2\text{O}_3$  after calcination and subsequent nitridation under an  $\text{NH}_3$  and  $\text{H}_2$  atmosphere, and CrN nanocubes (NCs) were generated. In the LSV curves, the current density under  $\text{N}_2$  was higher than that under Ar, indicating that CrN NCs are active for NRR. After a chronoamperometry (CA) test for 2 h, CrN NCs recorded an  $\text{NH}_3$  yield of  $31.11 \mu\text{g mg}_{\text{cat}}^{-1} \text{ h}^{-1}$  with an FE of 16.64% at  $-0.5 \text{ V}$ . In the control experiments (at open circuit potential under  $\text{N}_2$  flow and  $-0.5 \text{ V}$  under Ar flow), the produced amounts of ammonia were negligible. Furthermore, there were only small variations of FE and  $\text{NH}_3$  yields in the cycling tests that were repeated 5 times, showing the stability of CrN NCs for NRR. To understand the reaction based on the MvK mechanism, STEM-EDX analysis was conducted after the NRR tests of CrN NCs. The chemical composition showed an N-rich shell and an O-rich core. This is in contrast to what was expected to be an O-rich shell and N-rich core owing to the formation of oxide anions on the surface to replace nitride ions (leached from the lattice by the MvK mechanism). The authors explained that this resulted from the leaching of N atoms and consecutive rapid re-nitridation only at the surfaces, not the core.

Yao et al. synthesized  $\text{CrO}_x\text{N}_y$  via the urea-glass route [76]. The stoichiometry was estimated to be  $\text{CrO}_{0.66}\text{N}_{0.56}$  from STEM-EDS. For NRR tests, a proton exchange membrane electrolyzer (PEMEL) configuration was employed, using  $\text{CrO}_{0.66}\text{N}_{0.56}$  as a cathode and  $\text{IrO}_2$  as an anode. For the  $\text{CrO}_{0.66}\text{N}_{0.56}$  catalyst, the highest  $\text{NH}_3$  yield was found to be  $8.94 \times 10^{-11} \text{ mol s}^{-1} \text{ cm}^{-2}$ , and the highest FE of 6.7% was achieved at 2.0 V and 1.8 V, respectively (Figure 4b,c). Note that the measurements were conducted using an electrolytic cell. Meanwhile, the  $\text{Cr}_2\text{O}_3$  exhibited  $2.78 \times 10^{-11} \text{ mol s}^{-1} \text{ cm}^{-2}$  at 2.0 V and 2.8% at 1.8 V, implying that N-doping on chromium oxides can lead to better NRR activity. In addition, an  $\text{NH}_3$  yield of  $6.2 \times 10^{-11} \text{ mol s}^{-1} \text{ cm}^{-2}$  at 2.0 V was obtained on pure CrN; it was

assumed to come from the synergy effects between N and O atoms. In the XPS Cr<sub>3/2</sub> spectra, the binding energies of Cr<sup>3+</sup> and Cr<sup>6+</sup> species in CrO<sub>0.66</sub>N<sub>0.56</sub> shifted to higher energy levels compared to those in Cr<sub>2</sub>O<sub>3</sub> because of the electron transfer from Cr to N. Additionally, the binding energy of CrN (575.6 eV) is 1.5 eV lower than that of CrO<sub>0.66</sub>N<sub>0.56</sub> in the Cr<sub>3/2</sub> spectra, indicating a charge transfer from Cr to O. On the other hand, in the N-1s spectra, the binding energy of CrO<sub>0.66</sub>N<sub>0.56</sub> (397.9 eV) is higher than that of CrN (396.6 eV). The above results suggest that the enhanced charge transfers from Cr to O with respect to N. Thus, the N on CrN<sub>0.66</sub>N<sub>0.56</sub> can be reduced more easily than CrN, generating ammonia and N-vacancy. The crystallinity and surface states were not changed after a 3 h electrochemical test, verifying the stability of the CrO<sub>0.66</sub>N<sub>0.56</sub> catalysts for NRR.

### 3.1.3. Molybdenum Nitride-Based Catalysts

Zhang et al. prepared MoN nanosheets on carbon cloth (MoN NA/CC) as a catalyst for NRR [36]. A mixture of Na<sub>2</sub>MoO<sub>4</sub> and thiourea was hydrothermally treated with the CC substrate, and subsequent nitridation at 800 °C for 3 h generated the MoN NA/CC. The nanosheet structure of the catalyst was observed by TEM. The NRR performance of the MoN NA/CC in 0.1 M HCl solution recorded an FE of 1.15% and an NH<sub>3</sub> yield of  $3.01 \times 10^{-10}$  mol s<sup>-1</sup> cm<sup>-2</sup> at -0.3 V with no hydrazine generation. Furthermore, the MoN NA/CC showed good stability in 7 successive cycling tests and long-term durability tests over 27 h at -0.3 V. In addition, there was no correlation between N<sub>2</sub> flow rates and NRR performance, indicating that NRR is not dependent on the gas-solid interface (Figure 4d). After a long-term reaction of 62 h, the absence of the N atoms in MoN under the Ar atmosphere was identified by the XPS and EDX spectra, while the maintenance of N in MoN was determined under the N<sub>2</sub> atmosphere. Additionally, XRD patterns indicated metallic Mo formation after 62 h under Ar flow. These results suggest that the MoN NA/CC catalyzes NRR via the MvK mechanism. The detection of triplet <sup>14</sup>NH<sub>4</sub><sup>+</sup> and doublet <sup>15</sup>NH<sub>4</sub><sup>+</sup> signals in NMR using <sup>15</sup>N<sub>2</sub> results further confirmed that NRR followed the MvK mechanism.

A Mo<sub>2</sub>N nanorod was prepared by nitridation of MoO<sub>2</sub> at 700 °C for 3 h and used as an NRR catalyst in a 0.1 M HCl electrolyte [77]. The catalyst was loaded on the glassy carbon electrode (GCE) and acted as a working electrode. At -0.3 V, Mo<sub>2</sub>N/GCE showed an NH<sub>3</sub> yield of 78.4 μg mg<sub>cat</sub><sup>-1</sup> h<sup>-1</sup> and FE of 4.5%, while MoO<sub>2</sub>/GCE exhibited an NH<sub>3</sub> yield of 16.8 μg mg<sub>cat</sub><sup>-1</sup> h<sup>-1</sup> with an FE of 1.3%. These results indicate that N plays a critical role in NRR. Indeed, DFT calculations reveal that the free energy barrier of the potential determining step (PDS) of NRR on MoO<sub>2</sub> decreases dramatically after nitrogenization. For the MoO<sub>2</sub> catalyst, reductive protonation of the adsorbed N<sub>2</sub> (\*N<sub>2</sub>) to \*NNH is the PDS requiring 1.26 eV. However, for Mo<sub>2</sub>N, reductive protonation of \*NH in the second NH<sub>3</sub> formation is suggested as the PDS with a free energy of 0.66 eV. The FE and yield decreased below -0.3 V due to the competitive HER, which was proven by gas chromatography (GC). The produced amount of H<sub>2</sub> at -0.1 V and -0.2 V was much less than 5 μmol, and the corresponding FE was about 30%. However, at more negative than -0.3 V, H<sub>2</sub> production increased dramatically with an FE of 80%. The Mo<sub>2</sub>N/GCE showed no obvious performance decay during the recycling tests for 10 times and long-term reactions for 20 h, proving good stability for the NRR.

Yang et al. studied the role of cation vacancy for NRR by fabricating MoN nanocrystals with abundant Mo vacancy [78]. Mo-vacancy rich MoN nanocrystal on hierarchical porous carbon frame (MV-MoN@NC) is synthesized by annealing the mixture of SiO<sub>2</sub> spheres, molybdic acid, and dicyandiamide (DCDA) under NH<sub>3</sub> and Ar flow, and then MoN@NC connected with SiO<sub>2</sub> is formed. In the chemical etching process of SiO<sub>2</sub> by HF, the Si-O-Mo connection is easily removed, and the Mo vacancies are made on the MoN surface (Figure 4e). For comparison, MoN@NC is also synthesized with the same procedure, except that a polystyrene (PS) sphere was used instead of the SiO<sub>2</sub> sphere. The MV-MoN@NC showed a 3D honeycomb structure with ~500 nm cavities, and abundant defects in the MV-MoN@NC are observed in TEM images. The electron paramagnetic resonance (EPR)

results further verify the defects in the catalyst. In the EPR results, the intensity of the MV-MoN@NC peak is larger and wider than that of MoN@NC, indicating that it has more defects due to the unpaired electrons in the nitrogen atoms of MV-MoN@NC (Figure 4f). The MV-MoN@NC achieved the FE of 6.9% with an  $\text{NH}_3$  yield of  $76.9 \mu\text{g mg}_{\text{cat}}^{-1} \text{h}^{-1}$  at  $-0.2 \text{ V}$  in a  $0.1 \text{ M HCl}$  solution. The MoN@NC showed lower NRR performance with an  $\text{NH}_3$  yield of  $31.1 \mu\text{g mg}^{-1} \text{h}^{-1}$ . After the  $^{15}\text{N}_2$  isotope test, the MvK mechanism on MV-MoN@NC was identified by detecting both  $^{15}\text{NH}_4^+$  and  $^{14}\text{NH}_4^+$  signals in NMR spectra. The enhanced NRR performance on MV-MoN@NC was investigated by DFT calculations. For the MoN (200) surface, the PDS is the reduction step of  $^*\text{NH}$  to  $^*\text{NH}_2$ , with a relatively large energy barrier of  $1.40 \text{ eV}$ . In contrast, for the MoN (200) surface with Mo vacancies, the reductive protonation of  $^*\text{NH}_2$  to  $^*\text{NH}_3$  is the PDS, and its energy barrier is  $0.61 \text{ eV}$ . The reaction barrier,  $\Delta E$ , is inversely proportional to the reaction rate,  $k$ , by the Arrhenius equation. Therefore, the decrease of the energy barrier from  $1.40 \text{ eV}$  to  $0.61 \text{ eV}$  by the introduction of a Mo vacancy leads to an enhancement of the reaction rate, which results in better NRR performance.

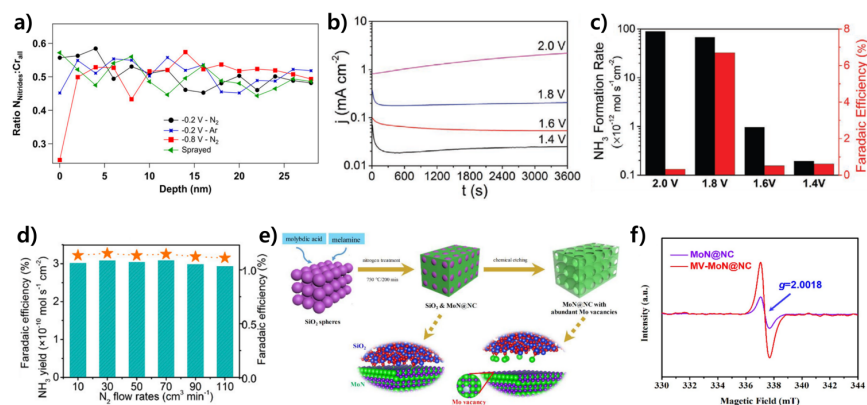


**Figure 4.** (a) The ratio of N to Cr in spent catalysts ( $\text{Cr}_2\text{N}$ ) through XPS-depth profiling. (b) J-t curves for 3 h at different potentials on  $\text{CrO}_{0.66}\text{N}_{0.56}$ . (c)  $\text{NH}_3$  formation rate with faradaic efficiency using  $\text{CrO}_{0.66}\text{N}_{0.56}$ . (d)  $\text{NH}_3$  yields and FEs with different  $\text{N}_2$  flow rates on MoN/CC at  $-0.3 \text{ V}$ . (e) Schematic illustration of MV-MoN@NC synthesis through the sacrificial-hard-template route. (f) EPR spectra of MV-MoN@NC and MoN@NC based on  $g = 2.0018$ . Reproduced with permission from the American Chemical Society [36,75], Wiley [76], and Elsevier [78].

### 3.1.4. Titanium Nitride-Based Catalysts

Commercial TiN was treated by ball-milling (TiN-BM) and subsequent plasma-etching (TiN-PE), and the generated titanium oxynitride ( $\text{TiO}_x\text{N}_y$ ) on TiN was pointed out as an NRR active phase [79]. The particle size of commercial TiN was  $1\text{--}3 \mu\text{m}$ , and the size decreased to  $100\text{--}500 \text{ nm}$  for TiN-BM. After the plasma-etching of TiN-BM, the surface morphology and particle size of TiN-PE were similar compared to TiN-BM. In comparison with TiN, the (200) peak in the XRD patterns of the TiN-PE moved to a lower angle due to the introduction of the larger O atoms relative to the N atoms. The introduction of O atoms was also observed in the Raman spectra. The peak intensity at  $130 \text{ cm}^{-1}$  (vibration of Ti-O) increased in TiN-PE compared to TiN-BM and TiN samples, suggesting plasma-etching treatment facilitates the formation of  $\text{TiO}_x\text{N}_y$  through surface oxidation of TiN. Likewise, in the XPS results, the nitrogen content of TiN-PE was lower, and the oxygen content of TiN-PE was higher than that of TiN-BM and TiN, which indicates that plasma-etching is effective for the introduction of high O content into the TiN structure, resulting in the formation of  $\text{TiO}_x\text{N}_y$ . With the TiN-PE, the electrochemical test was conducted in a  $0.1 \text{ M Na}_2\text{SO}_4$  solution, exhibiting an FE of 9.1% and an  $\text{NH}_3$  yield of  $3.32 \times 10^{-10} \text{ mol s}^{-1} \text{ cm}^{-2}$  at  $-0.6 \text{ V}$  (Figure 5a). Furthermore, the durability test conducted at  $-0.6 \text{ V}$  showed good stability for 12 h, and there was no significant change in  $\text{NH}_3$  yield and FE during 10 consecutive recycling tests. The time-dependent experiment of  $\text{NH}_3$



yield under an Ar-saturated electrolyte (3 h) and sequential N<sub>2</sub>-saturated electrolyte (3 h) supported the MvK mechanism on the TiN-PE. In the Ar-saturated electrolyte, the NH<sub>3</sub> yield initially slowly increased and stabilized at  $6.61 \times 10^{-11} \text{ mol s}^{-1} \text{ cm}^{-2}$  within 1 h. After the electrolyte was changed to an N<sub>2</sub>-saturated solution, the NH<sub>3</sub> yield increased rapidly, reaching  $3.95 \times 10^{-10} \text{ mol s}^{-1} \text{ cm}^{-2}$  after 3 h. The produced NH<sub>3</sub> in an Ar-saturated solution originated from TiO<sub>x</sub>N<sub>y</sub> in TiN-PE, i.e., the surface N atoms of TiO<sub>x</sub>N<sub>y</sub> were reduced to NH<sub>3</sub>, leaving N-vacancies. In an N<sub>2</sub>-saturated solution, subsequent adsorption and activation of N<sub>2</sub> on N-vacancies proceeded via the MvK mechanism, resulting in increased NH<sub>3</sub> yield. NMR results with the <sup>15</sup>N<sub>2</sub> isotope further confirmed that the NRR proceeded with the MvK mechanism, where doublet <sup>15</sup>NH<sub>4</sub><sup>+</sup> and triplet <sup>14</sup>NH<sub>4</sub><sup>+</sup> signals appeared together (Figure 5b).

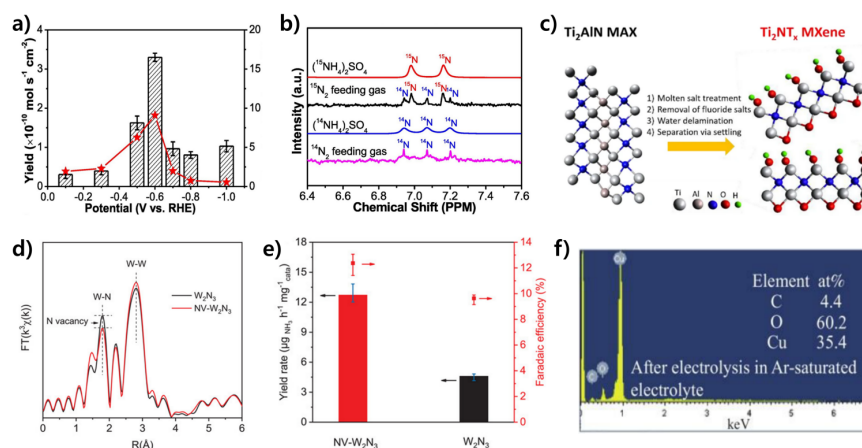


**Figure 5.** (a) NH<sub>3</sub> yield and FEs on TiN-PE. (b) <sup>1</sup>H NMR spectra for <sup>14</sup>NH<sub>4</sub><sup>+</sup>, <sup>15</sup>NH<sub>4</sub><sup>+</sup> from standard (<sup>14</sup>NH<sub>4</sub>)<sub>2</sub>SO<sub>4</sub>, (<sup>15</sup>NH<sub>4</sub>)<sub>2</sub>SO<sub>4</sub>, and <sup>14</sup>N<sub>2</sub>, <sup>15</sup>N<sub>2</sub> bubbled in electrolyte using TiN-PE. (c) A schematic illustration of the formation of Ti<sub>2</sub>N MXene from the Ti<sub>2</sub>AlN MAX phase. (d) FT-EXFAS plot of NV-W<sub>2</sub>N<sub>3</sub> and W<sub>2</sub>N<sub>3</sub>. (e) The difference between NV-W<sub>2</sub>N<sub>3</sub> and W<sub>2</sub>N<sub>3</sub> on NH<sub>3</sub> yield rate and FEs. (f) EDX analysis after electrolysis of Cu<sub>3</sub>N/CF in Ar-saturated electrolyte. Reproduced with permission from Springer Nature [80], Wiley [81], and Elsevier [79,82].

Two-dimensional Ti<sub>2</sub>N MXene was utilized for NRR with the expectation of a high surface area-to-volume ratio and easy access to N sites [80]. The Ti<sub>2</sub>AlN (MAX phase) was treated with a molten salt at 550 °C under Ar flow to form Ti<sub>2</sub>AlN-MST, and subsequent acid treatment for fluoride salt removal generates multi-layer Ti<sub>2</sub>N MXene (Ti<sub>2</sub>N-ML). Further exfoliation of Ti<sub>2</sub>N-ML by sonication in water produces only single layer Ti<sub>2</sub>N MXene (Ti<sub>2</sub>N-FL) (Figure 5c). The interlayer spacing of Ti<sub>2</sub>N-FL is three times higher than that of the MAX phase based on (002) peak position in XRD patterns, meaning that the clear separation of the layers from the MAX phase, in turn, increases the surface area by exposing more N sites, leading to enhanced NRR performance. The widened peaks because of the distortion of the structure caused by the electron density of the surface terminal group in the Raman analysis confirmed the transformation from the MAX phase to the MXene phase. The NRR activity of Ti<sub>2</sub>N-FL was compared with that of Ti<sub>3</sub>CN (carbonitride) and Ti<sub>3</sub>C<sub>2</sub> (carbide). In cyclic voltammetry (CV) measurements, Ti<sub>2</sub>N-FL and Ti<sub>3</sub>CN showed larger areas under N<sub>2</sub> than under Ar, indicating that more NH<sub>3</sub> could be generated because of the larger charge storage capacity. In the LSV curves, the current density of Ti<sub>2</sub>N-FL was about 10 times higher than that of Ti<sub>3</sub>CN due to a greater amount of N sites and improved reactivity. Considering that the Ti<sub>3</sub>C<sub>2</sub> showed limited NRR performance, the ratio of N atoms to Ti atoms within the lattice structure might affect the NRR performance. Ti<sub>2</sub>N-FL showed an FE of 19.85% and an NH<sub>3</sub> yield of  $11.33 \mu\text{g cm}^{-2} \text{ h}^{-1}$  at  $-0.25 \text{ V}$ . In contrast, Ti<sub>3</sub>CN exhibited an FE of 0.03% with an NH<sub>3</sub> yield of  $3.352 \mu\text{g cm}^{-2} \text{ h}^{-1}$  at  $-0.55 \text{ V}$ . NH<sub>3</sub> was not detected when a bare glassy carbon electrode without catalyst was used after a 4-hour CA test at  $-0.25 \text{ V}$ . On the other hand,

an  $\text{NH}_3$  yield of  $5.24 \mu\text{g cm}^{-2} \text{h}^{-1}$  was recorded at  $-0.25 \text{ V}$  under Ar flow, suggesting that NRR proceeds through the MvK mechanism.

### 3.1.5. Other TMN-Based Catalysts

Jin et al. used N-vacancy to introduce 2D-layered  $\text{W}_2\text{N}_3$  (NV- $\text{W}_2\text{N}_3$ ) in NRR [81]. The  $\text{W}_2\text{N}_3$  was prepared by nitridation of  $\text{Na}_2\text{W}_4\text{O}_{13}$  under an  $\text{NH}_3$  atmosphere, and additional annealing of  $\text{W}_2\text{N}_3$  under a 5%  $\text{H}_2/\text{Ar}$  atmosphere generates N-vacancies on the  $\text{W}_2\text{N}_3$  surface (NV- $\text{W}_2\text{N}_3$ ). In the XPS N-1s spectra, the peak intensity at 400.2 eV (assigned to N-vacancy) of NV- $\text{W}_2\text{N}_3$  increased compared to  $\text{W}_2\text{N}_3$ , suggesting a higher amount of N-vacancies on NV- $\text{W}_2\text{N}_3$ . Furthermore, the concentrations of the N-vacancies were calculated to be 6.6% for NV- $\text{W}_2\text{N}_3$  and 4.3% for  $\text{W}_2\text{N}_3$  based on the W/N atom ratio through XPS data. Additionally, in the W-L<sub>3</sub> edge in the extended X-ray absorption fine structure (EXFAS) spectra, the intensity of the peak for NV- $\text{W}_2\text{N}_3$  at 1.8 Å (W-N bonding) was reduced relative to  $\text{W}_2\text{N}_3$  (Figure 5d), implying a decreased coordination number of the W-N and thus, a formation of N-vacancies. The NV- $\text{W}_2\text{N}_3$  achieved an  $\text{NH}_3$  yield of  $3.80 \pm 0.32 \times 10^{-11} \text{ mol s}^{-1} \text{ cm}^{-2}$  with an FE of  $11.67 \pm 0.93\%$  at  $-0.2 \text{ V}$  in 0.1 M KOH. The  $\text{W}_2\text{N}_3$  showed a lower  $\text{NH}_3$  yield compared to the NV- $\text{W}_2\text{N}_3$ , revealing that N-vacancies affected the NRR activities (Figure 5e). During NRR measurements, hydrazine was not detected, and in the NMR test with the  $^{15}\text{N}_2$  isotope, only  $^{15}\text{NH}_4^+$  doublet signals were observed. These results suggest that the NRR on NV- $\text{W}_2\text{N}_3$  proceeded with the alternative distal mechanism, not the MvK mechanism. In DFT calculations, the release of the second  $\text{NH}_3$  is pointed out as the PDS for NV- $\text{W}_2\text{N}_3$ , pointing thermodynamically uphill with a free energy change of 0.97 eV. In comparison, the corresponding free energy change on  $\text{W}_2\text{N}$  is above 2 eV, verifying that the electron-deficient area induced by the N-vacancies can reduce the thermodynamic limiting potential and thus promote the NRR performance.

$\text{Cu}_3\text{N}/\text{CF}$  was prepared by a simple one-step synthesis as an NRR catalyst in a 0.1 M  $\text{Na}_2\text{SO}_4$  solution [82]. The Cu foam (downstream side) and urea (upstream side) were located separately on the alumina boat and annealed at  $300 \text{ }^\circ\text{C}$  under Ar flow. During the annealing process, urea can release ammonia, resulting in the growth of  $\text{Cu}_3\text{N}$  on the Cu foam. The  $\text{Cu}_3\text{N}/\text{CF}$  showed an  $\text{NH}_3$  yield of  $1.12 \times 10^{-10} \text{ mol s}^{-1} \text{ cm}^{-2}$ , and an FE of 1.5% at  $-0.2 \text{ V}$ . Bare Cu foam recorded an  $\text{NH}_3$  yield of  $1.0 \times 10^{-11} \text{ mol s}^{-1} \text{ cm}^{-2}$ . The  $C_{dl}$  values from CV measurements were  $12.4 \text{ mF cm}^{-2}$  for  $\text{Cu}_3\text{N}/\text{CF}$  and  $3.8 \text{ mF cm}^{-2}$  for Cu foam, suggesting that sheet-structured  $\text{Cu}_3\text{N}/\text{CF}$  had a wider electrochemically active surface area compared to Cu foam with a flat structure. The NRR activities of  $\text{Cu}_3\text{N}/\text{CF}$  were maintained after electrolysis for 14 h and 5 cycling tests. After an NRR test under Ar for 4 h, the N atoms on the surface of  $\text{Cu}_3\text{N}/\text{CF}$  disappeared from the EDX spectra, indicating the MvK mechanism (Figure 5f).

TMN-based composite catalysts were investigated in NRR to improve the performance of NRR.  $\gamma\text{-Mo}_2\text{N}$  nanoparticles on a 2D hexagonal boron nitride (h-BN) were prepared by one-step nitridation with molybdenum oxide, boric acid, and urea [83]. The initial amount of molybdenum oxide affected the size of the  $\text{Mo}_2\text{N}$  nanoparticle. Additionally, the larger the particle size, the more distorted the BN surface, creating B and N vacancies. The Mo atoms in  $\gamma\text{-Mo}_2\text{N}$  hybridize with  $\text{N}_2$  by receiving the electron lone pair for which the electron-deficient nitrogen vacancies could draw electrons. In compensation, Mo atoms donate the electron to adsorbed  $\text{N}_2$  molecules through  $\pi$ -back donation for activation. Therefore, vacancy-driven electron transfer between  $\gamma\text{-Mo}_2\text{N}/\text{h-BN}$  and  $\text{N}_2$  weakens the triple bond in  $\text{N}_2$ , lowering the energy barrier and enhancing the faradaic efficiency. The composite  $\gamma\text{-Mo}_2\text{N}$  on 2D-h-BN catalysts showed an  $\text{NH}_3$  yield of  $35.9 \mu\text{g mg}^{-1} \text{ h}^{-1}$  and FE of 61.5% at  $-0.3 \text{ V}$  in a 0.1 M  $\text{Na}_2\text{SO}_4$  solution.

Single Bi atom-incorporated hollow TiN nanorods encapsulated in nitrogen-doped carbon (NC) layer supported on carbon cloth (NC/Bi SAs/TiN/CC) were prepared by a 4-step process composed of BiOI electrodeposition on TiN/CC, ligand exchange, electrodeposition of aniline film, and pyrolysis with dicyandiamide at  $900 \text{ }^\circ\text{C}$  in  $\text{N}_2$  flow [84]. The NC layers with 2 nm thickness were incorporated with single Bi atoms, which are coated

on the surface of TiN. The composite NC/Bi SAs/TiN/CC catalysts showed an NH<sub>3</sub> yield of 76.15  $\mu\text{g mg}_{\text{cat}}^{-1} \text{h}^{-1}$  at  $-0.8 \text{ V}$  and FE of 24.6% at  $-0.5 \text{ V}$  in a 0.1 M Na<sub>2</sub>SO<sub>4</sub> solution. In the NMR results, doublet <sup>15</sup>NH<sub>4</sub><sup>+</sup> and triplet <sup>14</sup>NH<sub>4</sub><sup>+</sup> signals were observed when using <sup>15</sup>N<sub>2</sub> and <sup>14</sup>N<sub>2</sub> as the feed gases, confirming that the NH<sub>3</sub> is produced from NRR. The DFT study suggests that there exists a strong synergistic effect between Bi SAs and TiN substrate, which could simultaneously promote the hydrogenation of N<sub>2</sub> molecules into NH<sub>3</sub> \* on the TiN substrate and the desorption of NH<sub>3</sub> \* from single atomic Bi sites and thus boost NRR. The NRR performances and experimental conditions of the TMN-based catalysts are summarized in Table 1.

**Table 1.** The NRR performances of TMN-based catalysts.

TMNs Catalyst	Electrolyte	Potential /V vs. RHE	Production Rate /mol s <sup>-1</sup> cm <sup>-2</sup>	FE /%	Isotope	Test Cell Condition	Ref
VN/CC	0.1 M HCl	-0.3	$2.48 \times 10^{-10}$	3.58	X	H-cell	[73]
VN/TM	0.1 M HCl	-0.5	$8.40 \times 10^{-11}$	2.25	O	H-cell	[74]
VN nanoparticles	-	-0.1	$3.3 \times 10^{-10}$	6.0	O	MEA	[37]
Cr <sub>2</sub> N	-	-0.2	$1.4 \times 10^{-11}$	0.58	O	MEA	[75]
CrN	0.1 M HCl	-0.5	$6.1 \times 10^{-11}$	16.6	X	H-cell	[38]
CrO <sub>0.66</sub> N <sub>0.56</sub>	-	2.0	$8.94 \times 10^{-11}$	6.7 (at 1.8 V)	X	PEMEL	[76]
MoN NA/CC	0.1 M HCl	-0.3	$3.01 \times 10^{-10}$	1.15	O	H-cell	[36]
Mo <sub>2</sub> N/GCE	0.1 M HCl	-0.3	$78.4 \mu\text{g mg}_{\text{cat}}^{-1} \text{h}^{-1}$	4.5	X	H-cell	[77]
MV-MoN@NC	0.1 M HCl	-0.2	$5.02 \times 10^{-10}$	6.9	O	H-cell	[78]
TiN-PE	0.1 M Na <sub>2</sub> SO <sub>4</sub>	-0.6	$3.32 \times 10^{-10}$	9.1	O	Two-compartment	[79]
Ti <sub>2</sub> N MXene	0.1 M HCl	-0.25	$1.85 \times 10^{-10}$	19.85	X	H-cell	[80]
2D layered W <sub>2</sub> N <sub>3</sub>	0.1 M KOH	-0.2	$3.8 \pm 0.32 \times 10^{-11}$	$11.67 \pm 0.93$	O	H-cell	[81]
Cu <sub>3</sub> N/CF	0.1 M Na <sub>2</sub> SO <sub>4</sub>	-0.2	$1.12 \times 10^{-10}$	1.5	X	H-cell	[82]
$\gamma$ -Mo <sub>2</sub> N on 2D-h-BN	0.1 M Na <sub>2</sub> SO <sub>4</sub>	-0.3	$35.9 \mu\text{g mg}_{\text{cat}}^{-1} \text{h}^{-1}$	61.5	X	H-cell	[83]
NC/Bi SAs/TiN/CC	0.1 M Na <sub>2</sub> SO <sub>4</sub>	-0.8	$75.15 \mu\text{g mg}_{\text{cat}}^{-1} \text{h}^{-1}$	24.6	O	H-cell	[84]

### 3.2. TMN-Based Catalysts with Non-Catalytic Activity (Leaching or Decomposition)

#### 3.2.1. Vanadium Nitride-Based Catalysts

Manjunatha reported chemically and electrochemically unstable VN for NRR [85]. The NRR measurements were conducted in acidic (0.1 M HCl), neutral (0.1 M Na<sub>2</sub>SO<sub>4</sub>), and alkaline (0.1 M KOH) media with a commercial VN catalyst. All experimental instruments were cleaned with acid, and a control experiment was conducted to prevent contamination from N-source. Significant leaching of V and N elements was observed in the chemical and electrochemical experiments using VN. Notably, the concentration of V in an alkaline solution after chemical leaching was 12 times higher compared to other solutions (Figure 6a). Again, after the electrochemical reaction, V-leaching was the most severe in alkaline media, followed by acid and neutral media. After a chemical and electrochemical test in an alkaline solution, O elements, which were not present in pristine VN, were generated on VN, as evidenced by EDX results. This might be due to the replenishment of the N-vacancies with OH<sup>-</sup> ions in an alkaline solution. In acid and neutral media, O elements were not detected on the VN catalyst by EDX. Thus, N-vacancies remained unoccupied, resulting in a decreased N content compared to pristine VN (Figure 6b). Chemical leaching showed a higher NH<sub>3</sub> yield in acidic solutions compared to neutral solutions. In contrast, electrochemical leaching showed a higher NH<sub>3</sub> yield in neutral media compared to an acidic solution. The HER generally occurs more easily under acidic conditions and generated H<sub>2</sub> bubbles can prevent contact between the surface of VN with the electrolyte, thereby protecting V and N from dissolution. Therefore, the authors claimed that the chemical and electrochemical instability of VN limits the application of NRR due to the influence of NH<sub>3</sub> produced by N-leaching.

Du et al. also reported VN as an inactive catalyst for NRR [86]. The V(OH)<sub>x</sub> precursor was prepared by microwave radiation of VCl<sub>3</sub> and urea, which was then annealed at 600 °C under NH<sub>3</sub> flow to obtain the VN catalyst. Then, the VN was loaded onto carbon paper, which was used as electrode material. In CV tests under 0.05 M H<sub>2</sub>SO<sub>4</sub>, the current density

with  $N_2$  flow was higher compared to Ar flow. However, the amount of  $NH_3$  produced after CV was similar to the amount of  $NH_3$  produced after the CA test for 2 h at  $-0.6$  V under an  $N_2$ -saturated solution. Furthermore, a similar amount of  $NH_3$  was detected under the Ar-saturated solution after the CA test, suggesting that the produced  $NH_3$  was irrelevant to  $N_2$  gas and possibly originated from the lattice N atoms. In addition, adsorbed  $NH_3$  (which was absorbed on the catalyst surface after the electrochemical reaction) can be detected by soaking the electrode. The adsorbed  $NH_3$  was detected even without an applied potential under an Ar-saturated solution, provided that the produced  $NH_3$  is not related to the electrochemical reaction but mainly related to the unaided decomposition of the catalyst (i.e., the stability of the catalyst). For further confirmation, consecutive tests were conducted. In the 1st test with  $N_2$ ,  $NH_3$  was generated ( $17 \text{ mmol mol}_{\text{cat}}^{-1}$ ) after the CV test. However, during the subsequent CA test for 2 h, no  $NH_3$  was produced. Just a few “adsorbed”  $NH_3$  molecules were released ( $5 \text{ mmol mol}_{\text{cat}}^{-1}$ ) by soaking the electrode. In the 2nd test with Ar and the 3rd test with  $N_2$ , the trend is identical to the 1st test, meaning that  $NH_3$  was detected only after the CV test and no  $NH_3$  was produced after the subsequent CA test. Notably, the produced amount of  $NH_3$  gradually decreased as the tests proceeded from the 1st to the 3rd, suggesting the losses of surface N sites of VN. After these tests, a new peak at 402 eV corresponding to adsorbed ammonia or another form of protonated nitrogen was detected in the XPS N-1s spectra, indicating that N-vacancies cannot accept  $N_2$  continuously from the electrolyte and thus, VN cannot catalyze the NRR.

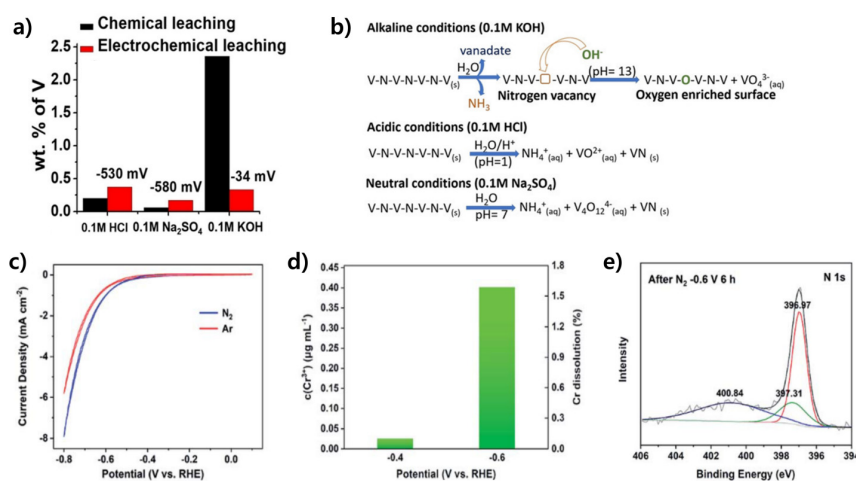


**Figure 6.** (a) Comparison of leached vanadium in VN after chemical and electrochemical reactions in acidic, neutral, and alkaline media. (b) The proposed  $NH_3$  production mechanism of VN in each condition. (c) CV curves of CrN NPs under  $N_2$ - and Ar-saturated solutions. (d)  $Cr^{3+}$  concentration and dissolution ratio at  $-0.4$  V and  $-0.6$  V for 1 h electrolysis. (e) XPS N-1s spectra after electrolysis for 6 h at  $-0.6$  V. Reproduced with permission from Wiley [85] and the Royal Society of Chemistry [87].

### 3.2.2. Chromium Nitride-Based Catalysts

The stability of lattice N and the deactivation path of CrN nanoparticles (CrN NP) were investigated [87]. Through the nitridation of the Cr-urea xerogel precursor at  $600$  °C in the  $NH_3$  atmosphere, the CrN NP was prepared. In the CV results of CrN NP, the current density in  $N_2$  was higher than that in Ar with negligible HER activity, which indicates that CrN is active for NRR (Figure 6c). After conducting CA tests for 1 h, an FE of 15.12% with an  $NH_3$  yield of  $7.47 \mu\text{g h}^{-1} \text{mg}^{-1}$  was achieved at  $-0.5$  V. At potentials below  $-0.6$  V, the FE and  $NH_3$  yield decreased because of the increased HER activity and N atom loss from the CrN lattice. Notably, produced  $NH_3$  was detected at all potentials under Ar flow, suggesting unavoidable lattice N leakage from CrN. To identify the stability of lattice N, cycling tests were carried out at  $-0.4$  V and  $-0.6$  V. During 6 consecutive tests for 1 h, there were continuous decreases in activity at both potentials, and the tendency of activity

decay was alleviated from the third cycle with steady  $\text{NH}_3$  production. At the end of the cycle, the  $\text{NH}_3$  yields at both potentials were similar, which was insufficient to explain the potential-induced changes. To find out other reasons for the activity decay according to the potentials, inductively coupled plasma-mass spectroscopy (ICP-MS) was employed, which revealed that the overall collapse of the structure is an important reason for the decay. The detected amount of  $\text{Cr}^{3+}$  at  $-0.6$  V was 20 times higher than that measured at  $-0.4$  V (Figure 6d), indicating that a more negative potential accelerates the collapse of the structure. In the XPS results conducted after the cycling test, the N/Cr ratios were determined to be 4.35 at  $-0.4$  V and 3.34 at  $-0.6$  V, which were much higher than the 0.57 of fresh CrN. The N/Cr ratio incensement was due to the adsorbed  $\text{NH}_3$  on the catalyst surface, as identified by the peak at 400 eV in the XPS N-1s spectra (Figure 6e). In the  $\text{NH}_3$ -TPD experiments, adsorbed  $\text{NH}_3$  on CrN was desorbed at  $658$  °C, revealing that the bond between CrN and  $\text{NH}_3$  is strong, and thus the strong bond between the CrN surface and  $\text{NH}_3$  resulted in catalyst poisoning. Hence, two possible deactivation mechanisms were suggested in this research: one is a potential-induced overall collapse of the structure, and the other is  $\text{NH}_3$  poisoning of the CrN.

### 3.2.3. Molybdenum Nitride-Based Catalysts

Hu et al. synthesized a  $\text{Mo}_2\text{N}$  catalyst via the urea-glass route as a catalyst for NRR, which showed a pure tetragonal  $\text{Mo}_2\text{N}$  crystalline structure [88]. Titanium (Ti) was selected as a substrate due to its inactivity for HER. Electrochemical tests were conducted in  $\text{N}_2$ - and Ar-saturated 0.1 M HCl solutions. At potentials below  $-0.22$  V, the current density in the  $\text{N}_2$ -saturated solution was slightly higher compared to the Ar-saturated solution in the LSV curves. The  $\text{Mo}_2\text{N}$ -loaded Ti ( $\text{Mo}_2\text{N}@\text{Ti}$ ) catalyst exhibited an FE of 42.3% with an  $\text{NH}_3$  yield of  $1.99 \mu\text{g mg}^{-1} \text{h}^{-1}$  at  $-0.05$  V and an FE of 28.4% with an  $\text{NH}_3$  yield of  $2.73 \mu\text{g mg}^{-1} \text{h}^{-1}$  at 0.05 V. At  $-0.15$  V, the FE substantially decreased to 1.93%. However, in the NMR tests using  $^{15}\text{N}_2$  gas, only  $^{14}\text{NH}_4^+$  triplet signals were observed without the  $^{15}\text{NH}_4^+$  doublet signals, which implies that the produced  $\text{NH}_3$  originated not from the catalytic reaction but from the decomposition of  $\text{Mo}_2\text{N}$  (Figure 7a). Even after incubating the  $\text{Mo}_2\text{N}@\text{Ti}$  electrode for 1 h without bias, a similar amount of  $\text{NH}_3$  was produced in all electrolytes (0.1 M HCl, 0.5 M NaCl, and 0.1 M NaOH) compared to the  $\text{NH}_3$  amount measured after the reaction at 0.05 V (Figure 7b). These results indicate the decomposition of  $\text{Mo}_2\text{N}$  in aqueous media. Moreover, it had a more severe instability in the alkaline solution and was dissolved entirely after 1 week of incubation in 0.1 M NaOH.

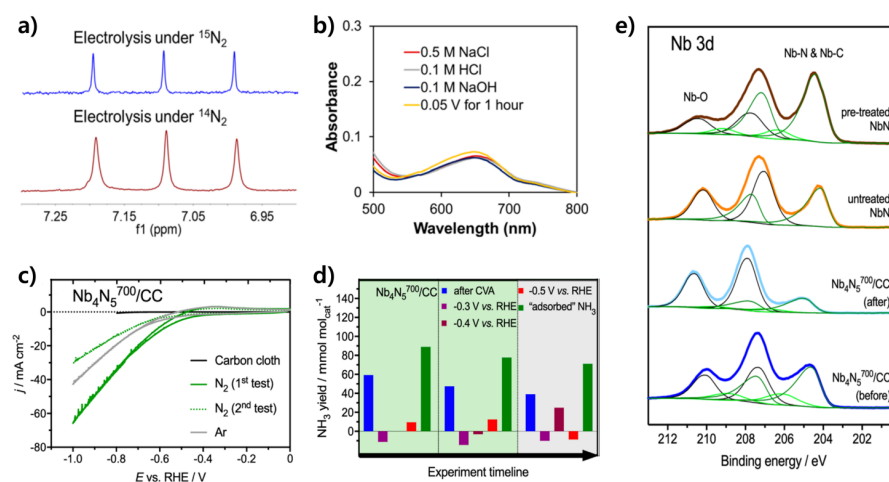


**Figure 7.** (a)  $^1\text{H}$  NMR spectra of  $^{14}\text{N}_2$  and  $^{15}\text{N}_2$  on  $\text{Mo}_2\text{N}$ . (b) Quantification of ammonia after incubating  $\text{Mo}_2\text{N}$  in acidic, neutral, and alkaline solutions without and with a bias for 1 h. (c) J-V curves on  $\text{Nb}_4\text{N}_5/\text{CC}$  in consecutive tests (1st— $\text{N}_2$ , 2nd— $\text{N}_2$ , 3rd—Ar). (d) Changes of produced  $\text{NH}_3$  for 3 times of consecutive tests. (e) XPS spectra in the Nb 3d region. Reproduced with permission from the American Chemistry Society [86,88].

### 3.2.4. Niobium Nitride-Based Catalysts

Du et al. investigated the non-catalytic activity of NbN and Nb<sub>4</sub>N<sub>5</sub> for NRR [86]. The NbN catalyst was prepared by the urea-glass route, and the particles are clustered due to the high annealing temperature (1000 °C). On the surface of NbN, oxide species, as well as nitrides, were detected by XPS resulting from the unavoidable surface oxidation. The surface oxide species of the NbN were removed by H<sub>3</sub>PO<sub>4</sub> treatment and tested for NRR. CV and CA tests were conducted in acidic, neutral, and alkaline media. Although the specific surface area of the NbN was low, the NbN loaded on the electrode was sufficient to produce NH<sub>3</sub>. However, NH<sub>3</sub> was just marginally produced, indicating that the NbN has no catalytic activity for NRR. Because of the high synthetic temperature of 1000 °C, NbN possesses a highly stable structure that cannot generate surface N-vacancies. Meanwhile, Nb<sub>4</sub>N<sub>5</sub> on carbon cloth (Nb<sub>4</sub>N<sub>5</sub>/CC) was synthesized by microwave irradiation at 200 °C and subsequent annealing at 700 °C under an NH<sub>3</sub> atmosphere. For the Nb<sub>4</sub>N<sub>5</sub>/CC, the produced amount of NH<sub>3</sub> after the CV test in a 0.05 M H<sub>2</sub>SO<sub>4</sub> solution was similar under N<sub>2</sub> and Ar flows, suggesting that NH<sub>3</sub> might be produced from the release of N atoms in the crystal lattice. This can be explained by the MvK mechanism without a catalytic reaction. The generated NH<sub>3</sub> in the first step originates from the surface nitrogen, leaving an N vacancy. However, the N-vacancy is blocked by other species and not replenished by N<sub>2</sub>. Hence, it does not proceed as a catalytic reaction. In addition, adsorbed ammonia was produced not only after the electrochemical reaction but also when no potential was applied, suggesting that it was also affected by the decomposition of the catalyst. Over 3 consecutive tests (each test includes the amount of NH<sub>3</sub> after CV and adsorbed NH<sub>3</sub>), the NH<sub>3</sub> yield decreased from the first to the third test (Figure 7c,d). In the first test, the amount of adsorbed NH<sub>3</sub> (90 mmol mol<sub>cat</sub><sup>-1</sup>) was higher than the amount after CV (60 mmol mol<sub>cat</sub><sup>-1</sup>), and it repeated during the tests, suggesting an instability of the Nb<sub>4</sub>N<sub>5</sub>. After the 3 consecutive tests, the physicochemical properties of the Nb<sub>4</sub>N<sub>5</sub>/CC have changed compared to the fresh catalyst. The morphology was unevenly agglomerated in the SEM images, and the crystalline peaks weakened in XRD. In the XPS results, the intensity of the peak around 204~205 eV for Nb<sub>4</sub>N<sub>5</sub> in the Nb 3d spectra decreased, and the peak intensities regarding oxygen species (207~208 eV) increased (Figure 7e). In the N 1s spectra, a peak at 402 eV corresponding to adsorbed ammonia was generated. The characterization results for Nb<sub>4</sub>N<sub>5</sub>/CC indicate weak structural stability during the electrochemical reaction, implying that Nb<sub>4</sub>N<sub>5</sub>/CC is not suitable for NRR.

## 4. Summary and Perspective

NH<sub>3</sub> is an indispensable chemical in various industrial fields. The most commonly employed method for NH<sub>3</sub> production is the HB process, which consumes a lot of energy with heavy CO<sub>2</sub> emissions. The NRR is a promising alternative to produce NH<sub>3</sub> to overcome the shortcomings of the HB process. Despite the merits of NRR, including environmental friendliness with carbon neutrality and cost-effectiveness with reduced energy consumption, insufficient FE and low NH<sub>3</sub> yields still limit its practical application. Obviously, the development of highly active and durable catalysts is of the utmost importance to realizing NRR at a practical level. In this review, we have summarized the recent research progress of TMN-based catalysts for NRR and provided information on their mechanism, synthetic routes, and characterization methods. Furthermore, contrasting views were considered, which indicated the inadequacy of the TMN-based catalysts for NRR due to chemical and electrochemical instability.

To produce NH<sub>3</sub> electrochemically using TMN-based catalysts, the following points should be considered: First, the rigorous procedure to detect NH<sub>3</sub> suggested by Chorkendorff and Simonov should be employed [89,90]. As we have introduced, there exists a controversial issue in the NRR activity of TMN-based catalysts (MvK mechanism or leaching). Furthermore, during the synthetic procedure of the TMN-based catalysts, N-containing chemicals are vitally used and can be a cause for false positives, influencing the NH<sub>3</sub> yield. Accordingly, careful control experiments should be conducted, especially

for the TMN-based catalysts, to identify the origin of the  $\text{NH}_3$  and quantify the amount of  $\text{NH}_3$  produced. The  $^{15}\text{N}_2$  isotope test can provide a distinct clue as to whether  $\text{NH}_3$  is produced from the supplied  $\text{N}_2$  gas. Indeed,  $^{15}\text{N}_2$  experiments are becoming imperative to ensure the reliability of the NRR results since 2019. On the other hand, to verify that the produced  $\text{NH}_3$  originated from the leaching of the TMN-based catalysts, additional experiments, such as ICP-OES, are suggested to measure the concentration of metal ions and correlate them with the produced amount of  $\text{NH}_3$ .

Second, the NRR mechanism should be further investigated in detail using advanced in situ characterization techniques. The NRR is a complex process involving multiple proton-coupled electron transfer steps, generating various intermediates on the catalyst surface. Thereby, the NRR mechanism has not been deeply understood so far, and currently, proposed mechanisms are mainly dependent on the computational simulation. Advanced in situ techniques, such as in situ Raman spectroscopy or in situ XAS, could provide useful information regarding the reaction intermediates, active sites, and, thus, NRR mechanism. By combining in situ characterization techniques with computational simulations, the development of highly efficient catalysts for NRR might be more achievable.

The above first and second points could help to clarify the debate regarding the origin of produced  $\text{NH}_3$  on TMN-based catalysts in the NRR. The third point is designing TMN-based catalysts with high activity and stability for NRR. To facilitate the NRR (via the MvK mechanism) while suppressing the inevitable competing HER reaction, several strategies can be considered. Defect engineering, including heteroatom doping and N-vacancy formation, can modify the electronic structures (i.e., intrinsic activity), regulating the binding energies of  $\text{N}_2$  and intermediates [91–93]. Additionally, morphology engineering techniques such as 2D materials, single-atom catalysts, facet-controlled catalysts, and composite catalysts (with catalyst supports) can help to increase the NRR activity by exposing more active sites and improving the contact area with the electrolyte.

Advanced system engineering is necessary in addition to catalyst design to enhance the NRR performance. The low solubility of  $\text{N}_2$  ( $0.0126 \text{ mg}\cdot\text{g}^{-1}$ ) in  $\text{H}_2\text{O}$  results in a low concentration of  $\text{N}_2$  molecules near the catalyst surface in an aqueous electrolyte system, resulting in low FE and  $\text{NH}_3$  yields. One effective solution is the use of a gas diffusion electrode (GDE) to increase the local  $\text{N}_2$  concentration and improve the NRR performance. Indeed, the design and implementation of GDE in NRR significantly affected its performances [23,94]. Moreover, the use of GDE can decrease the uncertainty by transferring low-current density aqueous electrolyte systems to high-current density practical GDE-based devices. Additionally, the GDE implementation can lead to a reduction in the cost of isotope experiments compared to the typical aqueous cell system by decreasing the required gas flow rate [95,96].

NRR is a strong option to produce  $\text{NH}_3$ , substituting the HB process. To realize the NRR at a practical level, highly active and durable catalysts for the NRR are crucial. Although the TMN-based catalysts are considered promising candidates due to their unique MvK mechanism, a careful approach is required because of the controversial views on the origin of the produced  $\text{NH}_3$ . By combining a rigorous procedure for  $\text{NH}_3$  detection and in situ characterizations, researchers can gain clear insight into the origin of  $\text{NH}_3$  and NRR mechanisms on the TMN-based catalysts. In turn, designing efficient TMN-based catalysts might be possible.

**Author Contributions:** Conceptualization, S.Y.P. and D.H.Y.; methodology, S.Y.P. and D.H.Y.; software, S.Y.P., Y.J.J. and D.H.Y.; validation, S.Y.P., Y.J.J. and D.H.Y.; investigation, S.Y.P., Y.J.J. and D.H.Y.; resources, Y.J.J. and D.H.Y.; data curation, S.Y.P. and D.H.Y.; writing—original draft preparation, S.Y.P., Y.J.J. and D.H.Y.; writing—review and editing, S.Y.P., Y.J.J. and D.H.Y.; visualization, S.Y.P., Y.J.J. and D.H.Y.; supervision, Y.J.J. and D.H.Y.; project administration, Y.J.J. and D.H.Y.; funding acquisition, D.H.Y. All authors have read and agreed to the published version of the manuscript.

**Funding:** This study was supported by the National Research Foundation of Korea (NRF) and grant-funded by the Korean government (Ministry of Education) (2019R1I1A3A01052741). This work was

also supported by the Korean Institute of Energy Technology Evaluation and Planning (KETEP) and the Ministry of Trade, Industry, and Energy (MOTIE) of the Republic of Korea (No. 2022400000080).

**Data Availability Statement:** Not applicable.

**Conflicts of Interest:** The authors declare no conflict of interest.

## References

1. Ghavam, S.; Vahdati, M.; Wilson, I.; Styring, P. Sustainable ammonia production processes. *Front. Energy Res.* **2021**, *9*, 34. [[CrossRef](#)]
2. Afif, A.; Radenahmad, N.; Cheok, Q.; Shams, S.; Kim, J.H.; Azad, A.K. Ammonia-fed fuel cells: A comprehensive review. *Renew. Sustain. Energy Rev.* **2016**, *60*, 822–835. [[CrossRef](#)]
3. Erisman, J.W.; Sutton, M.A.; Galloway, J.; Klimont, Z.; Winiwarter, W. How a century of ammonia synthesis changed the world. *Nat. Geosci.* **2008**, *1*, 636–639. [[CrossRef](#)]
4. Bird, F.; Clarke, A.; Davies, P.; Surkovic, E. Ammonia: Zero-Carbon Fertiliser, Fuel and Energy Store. In *The Royal Society; Policy Briefing*: London, UK, 2020.
5. Wang, X.; Yang, J.; Salla, M.; Xi, S.; Yang, Y.; Li, M.; Zhang, F.; Zhu, M.K.; Huang, S.; Huang, S. Redox-Mediated Ambient Electrolytic Nitrogen Reduction for Hydrazine and Ammonia Generation. *Angew. Chem. Int. Ed.* **2021**, *60*, 18721–18727. [[CrossRef](#)]
6. Guo, X.; Zhu, Y.; Ma, T. Lowering reaction temperature: Electrochemical ammonia synthesis by coupling various electrolytes and catalysts. *J. Energy Chem.* **2017**, *26*, 1107–1116. [[CrossRef](#)]
7. Chatterjee, S.; Parsapur, R.K.; Huang, K.-W. Limitations of Ammonia as a Hydrogen Energy Carrier for the Transportation Sector. *ACS Energy Lett.* **2021**, *6*, 4390–4394. [[CrossRef](#)]
8. Yang, B.; Ding, W.; Zhang, H.; Zhang, S. Recent progress in electrochemical synthesis of ammonia from nitrogen: Strategies to improve the catalytic activity and selectivity. *Energy Environ. Sci.* **2021**, *14*, 672–687. [[CrossRef](#)]
9. Humphreys, J.; Lan, R.; Tao, S. Development and recent progress on ammonia synthesis catalysts for Haber–Bosch process. *Adv. Energy Sustain. Res.* **2021**, *2*, 2000043. [[CrossRef](#)]
10. Qing, G.; Ghazfar, R.; Jackowski, S.T.; Habibzadeh, F.; Ashtiani, M.M.; Chen, C.-P.; Smith III, M.R.; Hamann, T.W. Recent advances and challenges of electrocatalytic N<sub>2</sub> reduction to ammonia. *Chem. Rev.* **2020**, *120*, 5437–5516. [[CrossRef](#)]
11. Faria, J.A. Renaissance of ammonia synthesis for sustainable production of energy and fertilizers. *Curr. Opin. Green Sustain. Chem.* **2021**, *29*, 100466. [[CrossRef](#)]
12. Cao, N.; Zheng, G. Aqueous electrocatalytic N<sub>2</sub> reduction under ambient conditions. *Nano Res.* **2018**, *11*, 2992–3008. [[CrossRef](#)]
13. Guo, X.; Du, H.; Qu, F.; Li, J. Recent progress in electrocatalytic nitrogen reduction. *J. Mater. Chem. A* **2019**, *7*, 3531–3543. [[CrossRef](#)]
14. Chen, J.G.; Crooks, R.M.; Seefeldt, L.C.; Bren, K.L.; Bullock, R.M.; Darensbourg, M.Y.; Holland, P.L.; Hoffman, B.; Janik, M.J.; Jones, A.K. Beyond fossil fuel–driven nitrogen transformations. *Science* **2018**, *360*, eaar6611. [[CrossRef](#)]
15. Smith, C.; Hill, A.K.; Torrente-Murciano, L. Current and future role of Haber–Bosch ammonia in a carbon-free energy landscape. *Energy Environ. Sci.* **2020**, *13*, 331–344. [[CrossRef](#)]
16. Bicer, Y.; Dincer, I.; Zamfirescu, C.; Vezina, G.; Raso, F. Comparative life cycle assessment of various ammonia production methods. *J. Clean. Prod.* **2016**, *135*, 1379–1395. [[CrossRef](#)]
17. Egenhofer, C.; Schrefler, L.; Rizos, V.; Marcu, A.; Genoese, F.; Renda, A.; Wiczorkiewicz, J.; Roth, S.; Infelise, F.; Luchetta, G. *The Composition and Drivers of Energy Prices and Costs in Energy-Intensive Industries: The Case of Ceramics, Glass and Chemicals*; Centre for European Policy Studies: Brussels, Belgium, 2014.
18. Service, R.F. Liquid sunshine. *Science* **2018**, *361*, 120–123. [[CrossRef](#)]
19. Wang, L.; Xia, M.; Wang, H.; Huang, K.; Qian, C.; Maravelias, C.T.; Ozin, G.A. Greening Ammonia toward the Solar Ammonia Refinery. *Joule* **2018**, *2*, 1055–1074. [[CrossRef](#)]
20. Bouckaert, S.; Pales, A.F.; McGlade, C.; Remme, U.; Wanner, B.; Varro, L.; D’Ambrosio, D.; Spencer, T. *Net Zero by 2050: A Roadmap for the Global Energy Sector*; International Energy Agency: Paris, France, 2021.
21. Tang, C.; Qiao, S.-Z. How to explore ambient electrocatalytic nitrogen reduction reliably and insightfully. *Chem. Soc. Rev.* **2019**, *48*, 3166–3180. [[CrossRef](#)]
22. Foster, S.L.; Bakovic, S.I.P.; Duda, R.D.; Maheshwari, S.; Milton, R.D.; Minter, S.D.; Janik, M.J.; Renner, J.N.; Greenlee, L.F. Catalysts for nitrogen reduction to ammonia. *Nat. Catal.* **2018**, *1*, 490–500. [[CrossRef](#)]
23. Hu, L.; Xing, Z.; Feng, X. Understanding the electrocatalytic interface for ambient ammonia synthesis. *ACS Energy Lett.* **2020**, *5*, 430–436. [[CrossRef](#)]
24. Li, S.-J.; Bao, D.; Shi, M.-M.; Wulan, B.-R.; Yan, J.-M.; Jiang, Q. Amorphizing of Au Nanoparticles by CeO<sub>x</sub>-RGO Hybrid Support towards Highly Efficient Electrocatalyst for N<sub>2</sub> Reduction under Ambient Conditions. *Adv. Mater.* **2017**, *29*, 1700001. [[CrossRef](#)] [[PubMed](#)]
25. Bao, D.; Zhang, Q.; Meng, F.-L.; Zhong, H.-X.; Shi, M.-M.; Zhang, Y.; Yan, J.-M.; Jiang, Q.; Zhang, X.-B. Electrochemical Reduction of N<sub>2</sub> under Ambient Conditions for Artificial N<sub>2</sub> Fixation and Renewable Energy Storage Using N<sub>2</sub>/NH<sub>3</sub> Cycle. *Adv. Mater.* **2017**, *29*, 1604799. [[CrossRef](#)] [[PubMed](#)]



26. Wang, D.; Azofra, L.M.; Harb, M.; Cavallo, L.; Zhang, X.; Suryanto, B.H.; MacFarlane, D.R. Energy-efficient nitrogen reduction to ammonia at low overpotential in aqueous electrolyte under ambient conditions. *ChemSusChem* **2018**, *11*, 3416–3422. [[CrossRef](#)] [[PubMed](#)]
27. Ruiyi, L.; Keyang, H.; Pengwu, X.; Wendong, W.; Nana, L.; Haiyan, Z.; Zaijun, L.; Xiaohao, L. Synthesis of a ruthenium–graphene quantum dot–graphene hybrid as a promising single-atom catalyst for electrochemical nitrogen reduction with ultrahigh yield rate and selectivity. *J. Mater. Chem. A* **2021**, *9*, 24582–24589. [[CrossRef](#)]
28. Huang, H.; Xia, L.; Shi, X.; Asiri, A.M.; Sun, X. Ag nanosheets for efficient electrocatalytic N<sub>2</sub> fixation to NH<sub>3</sub> under ambient conditions. *ChemComm* **2018**, *54*, 11427–11430. [[CrossRef](#)]
29. Li, W.; Li, K.; Ye, Y.; Zhang, S.; Liu, Y.; Wang, G.; Liang, C.; Zhang, H.; Zhao, H. Efficient electrocatalytic nitrogen reduction to ammonia with aqueous silver nanodots. *Commun. Chem.* **2021**, *4*, 10. [[CrossRef](#)]
30. Wang, X.; Luo, M.; Lan, J.; Peng, M.; Tan, Y. Nanoporous Intermetallic Pd<sub>3</sub>Bi for Efficient Electrochemical Nitrogen Reduction. *Adv. Mater.* **2021**, *33*, 2007733. [[CrossRef](#)]
31. Xie, H.; Geng, Q.; Zhu, X.; Luo, Y.; Chang, L.; Niu, X.; Shi, X.; Asiri, A.M.; Gao, S.; Wang, Z. PdP<sub>2</sub> nanoparticles–reduced graphene oxide for electrocatalytic N<sub>2</sub> conversion to NH<sub>3</sub> under ambient conditions. *J. Mater. Chem. A* **2019**, *7*, 24760–24764. [[CrossRef](#)]
32. Liu, H.-M.; Han, S.-H.; Zhao, Y.; Zhu, Y.-Y.; Tian, X.-L.; Zeng, J.-H.; Jiang, J.-X.; Xia, B.Y.; Chen, Y. Surfactant-free atomically ultrathin rhodium nanosheet nanoassemblies for efficient nitrogen electroreduction. *J. Mater. Chem. A* **2018**, *6*, 3211–3217. [[CrossRef](#)]
33. Liu, Y.; Zhu, X.; Zhang, Q.; Tang, T.; Zhang, Y.; Gu, L.; Li, Y.; Bao, J.; Dai, Z.; Hu, J.-S. Engineering Mo/Mo<sub>2</sub>C/MoC hetero-interfaces for enhanced electrocatalytic nitrogen reduction. *J. Mater. Chem. A* **2020**, *8*, 8920–8926. [[CrossRef](#)]
34. Feng, J.; Zhu, X.; Chen, Q.; Xiong, W.; Chen, X.; Luo, Y.; Alshehri, A.A.; Alzahrani, K.A.; Jiang, Z.; Li, W. Ultrasmall V<sub>8</sub>C<sub>7</sub> nanoparticles embedded in conductive carbon for efficient electrocatalytic N<sub>2</sub> reduction toward ambient NH<sub>3</sub> production. *J. Mater. Chem. A* **2019**, *7*, 26227–26230. [[CrossRef](#)]
35. Ren, X.; Zhao, J.; Wei, Q.; Ma, Y.; Guo, H.; Liu, Q.; Wang, Y.; Cui, G.; Asiri, A.M.; Li, B. High-performance N<sub>2</sub>-to-NH<sub>3</sub> conversion electrocatalyzed by Mo<sub>2</sub>C nanorod. *ACS Cent. Sci.* **2018**, *5*, 116–121. [[CrossRef](#)]
36. Zhang, L.; Ji, X.; Ren, X.; Luo, Y.; Shi, X.; Asiri, A.M.; Zheng, B.; Sun, X. Efficient electrochemical N<sub>2</sub> reduction to NH<sub>3</sub> on MoN nanosheets array under ambient conditions. *ACS Sustain. Chem. Eng.* **2018**, *6*, 9550–9554. [[CrossRef](#)]
37. Yang, X.; Nash, J.; Anibal, J.; Dunwell, M.; Kattel, S.; Stavitski, E.; Attenkofer, K.; Chen, J.G.; Yan, Y.; Xu, B. Mechanistic insights into electrochemical nitrogen reduction reaction on vanadium nitride nanoparticles. *J. Am. Chem. Soc.* **2018**, *140*, 13387–13391. [[CrossRef](#)]
38. Ma, Z.; Chen, J.; Luo, D.; Thersleff, T.; Dronskowski, R.; Slabon, A. Structural evolution of CrN nanocube electrocatalysts during nitrogen reduction reaction. *Nanoscale* **2020**, *12*, 19276–19283. [[CrossRef](#)]
39. Zhang, L.; Ji, X.; Ren, X.; Ma, Y.; Shi, X.; Tian, Z.; Asiri, A.M.; Chen, L.; Tang, B.; Sun, X. Electrochemical ammonia synthesis via nitrogen reduction reaction on a MoS<sub>2</sub> catalyst: Theoretical and experimental studies. *Adv. Mater.* **2018**, *30*, 1800191. [[CrossRef](#)]
40. Kong, J.; Kim, M.-S.; Akbar, R.; Park, H.Y.; Jang, J.H.; Kim, H.; Hur, K.; Park, H.S. Electrochemical nitrogen reduction kinetics on a copper sulfide catalyst for NH<sub>3</sub> synthesis at low temperature and atmospheric pressure. *ACS Appl. Mater. Interfaces* **2021**, *13*, 24593–24603. [[CrossRef](#)]
41. Zhao, X.; Lan, X.; Yu, D.; Fu, H.; Liu, Z.; Mu, T. Deep eutectic-solvothermal synthesis of nanostructured Fe<sub>3</sub>S<sub>4</sub> for electrochemical N<sub>2</sub> fixation under ambient conditions. *ChemComm* **2018**, *54*, 13010–13013. [[CrossRef](#)]
42. Han, J.; Ji, X.; Ren, X.; Cui, G.; Li, L.; Xie, F.; Wang, H.; Li, B.; Sun, X. MoO<sub>3</sub> nanosheets for efficient electrocatalytic N<sub>2</sub> fixation to NH<sub>3</sub>. *J. Mater. Chem. A* **2018**, *6*, 12974–12977. [[CrossRef](#)]
43. Liu, Q.; Zhang, X.; Zhang, B.; Luo, Y.; Cui, G.; Xie, F.; Sun, X. Ambient N<sub>2</sub> fixation to NH<sub>3</sub> electrocatalyzed by a spinel Fe<sub>3</sub>O<sub>4</sub> nanorod. *Nanoscale* **2018**, *10*, 14386–14389. [[CrossRef](#)]
44. Kong, J.; Lim, A.; Yoon, C.; Jang, J.H.; Ham, H.C.; Han, J.; Nam, S.; Kim, D.; Sung, Y.-E.; Choi, J.; et al. Electrochemical Synthesis of NH<sub>3</sub> at Low Temperature and Atmospheric Pressure Using a γ-Fe<sub>2</sub>O<sub>3</sub> Catalyst. *ACS Sustain. Chem. Eng.* **2017**, *5*, 10986–10995. [[CrossRef](#)]
45. Mou, T.; Liang, J.; Ma, Z.; Zhang, L.; Lin, Y.; Li, T.; Liu, Q.; Luo, Y.; Liu, Y.; Gao, S.; et al. High-efficiency electrohydrogenation of nitric oxide to ammonia on a Ni<sub>2</sub>P nanoarray under ambient conditions. *J. Mater. Chem. A* **2021**, *9*, 24268–24275. [[CrossRef](#)]
46. Guo, W.; Liang, Z.; Zhao, J.; Zhu, B.; Cai, K.; Zou, R.; Xu, Q. Hierarchical cobalt phosphide hollow nanocages toward electrocatalytic ammonia synthesis under ambient pressure and room temperature. *Small Methods* **2018**, *2*, 1800204. [[CrossRef](#)]
47. Zhu, X.; Wu, T.; Ji, L.; Liu, Q.; Luo, Y.; Cui, G.; Xiang, Y.; Zhang, Y.; Zheng, B.; Sun, X. Unusual electrochemical N<sub>2</sub> reduction activity in an earth-abundant iron catalyst via phosphorous modulation. *ChemComm* **2020**, *56*, 731–734. [[CrossRef](#)]
48. Lan, J.; Luo, M.; Han, J.; Peng, M.; Duan, H.; Tan, Y. Nanoporous B<sub>13</sub>C<sub>2</sub> towards highly efficient electrochemical nitrogen fixation. *Small* **2021**, *17*, 2102814. [[CrossRef](#)]
49. Zhang, M.; Choi, C.; Huo, R.; Gu, G.H.; Hong, S.; Yan, C.; Xu, S.; Robertson, A.W.; Qiu, J.; Jung, Y.; et al. Reduced graphene oxides with engineered defects enable efficient electrochemical reduction of dinitrogen to ammonia in wide pH range. *Nano Energy* **2020**, *68*, 104323. [[CrossRef](#)]
50. Song, P.; Wang, H.; Kang, L.; Ran, B.; Song, H.; Wang, R. Electrochemical nitrogen reduction to ammonia at ambient conditions on nitrogen and phosphorus co-doped porous carbon. *ChemComm* **2019**, *55*, 687–690. [[CrossRef](#)]

51. MacFarlane, D.R.; Cherepanov, P.V.; Choi, J.; Suryanto, B.H.R.; Hodgetts, R.Y.; Bakker, J.M.; Ferrero Vallana, F.M.; Simonov, A.N. A Roadmap to the Ammonia Economy. *Joule* **2020**, *4*, 1186–1205. [[CrossRef](#)]
52. Chen, J.G. Carbide and Nitride Overlayers on Early Transition Metal Surfaces: Preparation, Characterization, and Reactivities. *Chem. Rev.* **1996**, *96*, 1477–1498. [[CrossRef](#)]
53. Yang, M.; Allen, A.J.; Nguyen, M.T.; Ralston, W.T.; MacLeod, M.J.; DiSalvo, F.J. Corrosion behavior of mesoporous transition metal nitrides. *J. Solid State Chem.* **2013**, *205*, 49–56. [[CrossRef](#)]
54. Marchand, R.; Tessier, F.; DiSalvo, F.J. New routes to transition metal nitrides: And characterization of new phases. *J. Mater. Chem.* **1999**, *9*, 297–304. [[CrossRef](#)]
55. Youn, D.H.; Bae, G.; Han, S.; Kim, J.Y.; Jang, J.-W.; Park, H.; Choi, S.H.; Lee, J.S. A highly efficient transition metal nitride-based electrocatalyst for oxygen reduction reaction: TiN on a CNT–graphene hybrid support. *J. Mater. Chem. A* **2013**, *1*, 8007–8015. [[CrossRef](#)]
56. Xie, J.; Xie, Y. Transition Metal Nitrides for Electrocatalytic Energy Conversion: Opportunities and Challenges. *Chem. Eur. J.* **2016**, *22*, 3588–3598. [[CrossRef](#)]
57. Dongil, A.B. Recent Progress on Transition Metal Nitrides Nanoparticles as Heterogeneous Catalysts. *Nanomaterials* **2019**, *9*, 1111. [[CrossRef](#)]
58. Dong, Y.; Deng, Y.; Zeng, J.; Song, H.; Liao, S. A high-performance composite ORR catalyst based on the synergy between binary transition metal nitride and nitrogen-doped reduced graphene oxide. *J. Mater. Chem. A* **2017**, *5*, 5829–5837. [[CrossRef](#)]
59. Luo, J.; Tian, X.; Zeng, J.; Li, Y.; Song, H.; Liao, S. Limitations and Improvement Strategies for Early-Transition-Metal Nitrides as Competitive Catalysts toward the Oxygen Reduction Reaction. *ACS Catal.* **2016**, *6*, 6165–6174. [[CrossRef](#)]
60. Go, H.; Akio, I.; Tsuyoshi, T.; Kondo, J.N.; Michikazu, H.; Kazunari, D. Ta<sub>3</sub>N<sub>5</sub> as a Novel Visible Light-Driven Photocatalyst ( $\lambda < 600$  nm). *Chem. Lett.* **2002**, *31*, 736–737.
61. Kim, J.Y.; Lee, M.H.; Kim, J.-H.; Kim, C.W.; Youn, D.H. Facile nanocrystalline Ta<sub>3</sub>N<sub>5</sub> synthesis for photocatalytic dye degradation under visible light. *Chem. Phys. Lett.* **2020**, *738*, 136900. [[CrossRef](#)]
62. Seol, M.; Youn, D.H.; Kim, J.Y.; Jang, J.-W.; Choi, M.; Lee, J.S.; Yong, K. Mo-Compound/CNT-Graphene Composites as Efficient Catalytic Electrodes for Quantum-Dot-Sensitized Solar Cells. *Adv. Energy Mater.* **2014**, *4*, 1300775. [[CrossRef](#)]
63. Youn, D.; Seol, M.; Kim, J.; Jang, J.-W.; Choi, Y.; Yong, K.; Lee, J.S. TiN Nanoparticles on CNT-Graphene Hybrid Support as Noble-Metal-Free Counter Electrode for Quantum-Dot-Sensitized Solar Cells. *ChemSusChem* **2013**, *6*, 261–267. [[CrossRef](#)]
64. Park, S.H.; Jo, T.H.; Lee, M.H.; Kawashima, K.; Mullins, C.B.; Lim, H.-K.; Youn, D.H. Highly active and stable nickel–molybdenum nitride (Ni<sub>2</sub>Mo<sub>3</sub>N) electrocatalyst for hydrogen evolution. *J. Mater. Chem. A* **2021**, *9*, 4945–4951. [[CrossRef](#)]
65. Park, S.H.; Kang, S.H.; Youn, D.H. Direct One-Step Growth of Bimetallic Ni<sub>2</sub>Mo<sub>3</sub>N on Ni Foam as an Efficient Oxygen Evolution Electrocatalyst. *Materials* **2021**, *14*, 4768. [[CrossRef](#)]
66. Abghoui, Y.; Garden, A.L.; Hlynsson, V.F.; Björgvinsdóttir, S.; Ólafsdóttir, H.; Skúlason, E. Enabling electrochemical reduction of nitrogen to ammonia at ambient conditions through rational catalyst design. *Phys. Chem. Chem. Phys.* **2015**, *17*, 4909–4918. [[CrossRef](#)] [[PubMed](#)]
67. Abghoui, Y.; Skúlason, E. Onset potentials for different reaction mechanisms of nitrogen activation to ammonia on transition metal nitride electro-catalysts. *Catal. Today* **2017**, *286*, 69–77. [[CrossRef](#)]
68. Abghoui, Y.; Skúlason, E. Transition Metal Nitride Catalysts for Electrochemical Reduction of Nitrogen to Ammonia at Ambient Conditions. *Procedia Comput. Sci.* **2015**, *51*, 1897–1906. [[CrossRef](#)]
69. Abghoui, Y.; Skúlason, E. Electrochemical synthesis of ammonia via Mars-van Krevelen mechanism on the (111) facets of group III–VII transition metal mononitrides. *Catal. Today* **2017**, *286*, 78–84. [[CrossRef](#)]
70. Abghoui, Y.; Garden, A.L.; Howalt, J.G.; Vegge, T.; Skúlason, E. Electroreduction of N<sub>2</sub> to Ammonia at Ambient Conditions on Mononitrides of Zr, Nb, Cr, and V: A DFT Guide for Experiments. *ACS Catal.* **2016**, *6*, 635–646. [[CrossRef](#)]
71. Gambarotta, S.; Scott, J. Multimetallic Cooperative Activation of N<sub>2</sub>. *Angew. Chem. Int. Ed.* **2004**, *43*, 5298–5308. [[CrossRef](#)]
72. Kitano, M.; Inoue, Y.; Yamazaki, Y.; Hayashi, F.; Kanbara, S.; Matsuiishi, S.; Yokoyama, T.; Kim, S.-W.; Hara, M.; Hosono, H. Ammonia synthesis using a stable electronegative as an electron donor and reversible hydrogen store. *Nat. Chem.* **2012**, *4*, 934–940. [[CrossRef](#)]
73. Zhang, X.; Kong, R.-M.; Du, H.; Xia, L.; Qu, F. Highly efficient electrochemical ammonia synthesis via nitrogen reduction reactions on a VN nanowire array under ambient conditions. *ChemComm* **2018**, *54*, 5323–5325. [[CrossRef](#)]
74. Zhang, R.; Zhang, Y.; Ren, X.; Cui, G.; Asiri, A.M.; Zheng, B.; Sun, X. High-Efficiency Electrosynthesis of Ammonia with High Selectivity under Ambient Conditions Enabled by VN Nanosheet Array. *ACS Sustain. Chem. Eng.* **2018**, *6*, 9545–9549. [[CrossRef](#)]
75. Nash, J.; Yang, X.; Anibal, J.; Dunwell, M.; Yao, S.; Attenkofer, K.; Chen, J.G.; Yan, Y.; Xu, B. Elucidation of the Active Phase and Deactivation Mechanisms of Chromium Nitride in the Electrochemical Nitrogen Reduction Reaction. *J. Phys. Chem. C* **2019**, *123*, 23967–23975. [[CrossRef](#)]
76. Yao, Y.; Feng, Q.; Zhu, S.; Li, J.; Yao, Y.; Wang, Y.; Wang, Q.; Gu, M.; Wang, H.; Li, H.; et al. Chromium Oxynitride Electrocatalysts for Electrochemical Synthesis of Ammonia Under Ambient Conditions. *Small Methods* **2019**, *3*, 1800324. [[CrossRef](#)]
77. Ren, X.; Cui, G.; Chen, L.; Xie, F.; Wei, Q.; Tian, Z.; Sun, X. Electrochemical N<sub>2</sub> fixation to NH<sub>3</sub> under ambient conditions: Mo<sub>2</sub>N nanorod as a highly efficient and selective catalyst. *ChemComm* **2018**, *54*, 8474–8477.
78. Yang, X.; Ling, F.; Su, J.; Zi, X.; Zhang, H.; Zhang, H.; Li, J.; Zhou, M.; Wang, Y. Insights into the role of cation vacancy for significantly enhanced electrochemical nitrogen reduction. *Appl. Catal. B* **2020**, *264*, 118477. [[CrossRef](#)]

79. Kang, S.; Wang, J.; Zhang, S.; Zhao, C.; Wang, G.; Cai, W.; Zhang, H. Plasma-etching enhanced titanium oxynitride active phase with high oxygen content for ambient electrosynthesis of ammonia. *Electrochem. Commun.* **2019**, *100*, 90–95. [[CrossRef](#)]
80. Johnson, D.; Hunter, B.; Christie, J.; King, C.; Kelley, E.; Djire, A. Ti<sub>2</sub>N nitride MXene evokes the Mars-van Krevelen mechanism to achieve high selectivity for nitrogen reduction reaction. *Sci. Rep.* **2022**, *12*, 657. [[CrossRef](#)] [[PubMed](#)]
81. Jin, H.; Li, L.; Liu, X.; Tang, C.; Xu, W.; Chen, S.; Song, L.; Zheng, Y.; Qiao, S.-Z. Nitrogen Vacancies on 2D Layered W<sub>2</sub>N<sub>3</sub>: A Stable and Efficient Active Site for Nitrogen Reduction Reaction. *Adv. Mater.* **2019**, *31*, 1902709. [[CrossRef](#)]
82. He, H.-y.; Wang, S.; Ji, L.-L. Fabrication of self-supported Cu<sub>3</sub>N electrode for electrocatalytic nitrogen reduction reaction. *J. Fuel Chem. Technol.* **2022**, *50*, 484–493. [[CrossRef](#)]
83. Yesudoss, D.K.; Lee, G.; Shanmugam, S. Strong catalyst support interactions in defect-rich  $\gamma$ -Mo<sub>2</sub>N nanoparticles loaded 2D-h-BN hybrid for highly selective nitrogen reduction reaction. *Appl. Catal. B Environ.* **2021**, *287*, 119952. [[CrossRef](#)]
84. Xi, Z.; Shi, K.; Xu, X.; Jing, P.; Liu, B.; Gao, R.; Zhang, J. Boosting Nitrogen Reduction Reaction via Electronic Coupling of Atomically Dispersed Bismuth with Titanium Nitride Nanorods. *Adv. Sci.* **2022**, *9*, 2104245. [[CrossRef](#)]
85. Manjunatha, R.; Karajić, A.; Teller, H.; Nicoara, K.; Schechter, A. Electrochemical and Chemical Instability of Vanadium Nitride in the Synthesis of Ammonia Directly from Nitrogen. *ChemCatChem* **2020**, *12*, 438–443. [[CrossRef](#)]
86. Du, H.-L.; Gengenbach, T.R.; Hodgetts, R.; MacFarlane, D.R.; Simonov, A.N. Critical Assessment of the Electrocatalytic Activity of Vanadium and Niobium Nitrides toward Dinitrogen Reduction to Ammonia. *ACS Sustain. Chem. Eng.* **2019**, *7*, 6839–6850. [[CrossRef](#)]
87. Guo, W.; Liang, Z.; Tang, Y.; Cai, K.; Qiu, T.; Wu, Y.; Zhang, K.; Gao, S.; Zou, R. Understanding the lattice nitrogen stability and deactivation pathways of cubic CrN nanoparticles in the electrochemical nitrogen reduction reaction. *J. Mater. Chem. A* **2021**, *9*, 8568–8575. [[CrossRef](#)]
88. Hu, B.; Hu, M.; Seefeldt, L.; Liu, T.L. Electrochemical Dinitrogen Reduction to Ammonia by Mo<sub>2</sub>N: Catalysis or Decomposition? *ACS Energy Lett.* **2019**, *4*, 1053–1054. [[CrossRef](#)]
89. Andersen, S.Z.; Čolić, V.; Yang, S.; Schwalbe, J.A.; Nielander, A.C.; McEnaney, J.M.; Enemark-Rasmussen, K.; Baker, J.G.; Singh, A.R.; Rohr, B.A.; et al. A rigorous electrochemical ammonia synthesis protocol with quantitative isotope measurements. *Nature* **2019**, *570*, 504–508. [[CrossRef](#)]
90. Choi, J.; Suryanto, B.H.R.; Wang, D.; Du, H.-L.; Hodgetts, R.Y.; Ferrero Vallana, F.M.; MacFarlane, D.R.; Simonov, A.N. Identification and elimination of false positives in electrochemical nitrogen reduction studies. *Nat. Commun.* **2020**, *11*, 5546. [[CrossRef](#)]
91. Wei, J.; Jing, Y.; Zhao, Z.; Fan, Z.; Liang, Z.; Huang, J.; Wu, H.; Xie, Z.; Liu, D.; Qu, D.; et al. Catalyst-Support interactions enhanced electrochemical nitrogen reduction on Au/ZrO<sub>2</sub>. *Electrochim. Acta* **2021**, *381*, 138222. [[CrossRef](#)]
92. Wang, J.; Wei, J.; An, C.; Tang, H.; Deng, Q.; Li, J. Electrocatalyst design for the conversion of energy molecules: Electronic state modulation and mass transport regulation. *Chem. Commun.* **2022**, *58*, 10907–10924. [[CrossRef](#)]
93. Ologunagba, D.; Kattel, S. A Density Functional Theory Study of Electrochemical Nitrogen Reduction to Ammonia on the (100) Surface of Transition-Metal Oxynitrides. *J. Phys. Chem. C* **2022**, *126*, 17045–17055. [[CrossRef](#)]
94. Wei, X.; Vogel, D.; Keller, L.; Kriescher, S.; Wessling, M. Microtubular Gas Diffusion Electrode Based on Ruthenium-Carbon Nanotubes for Ambient Electrochemical Nitrogen Reduction to Ammonia. *ChemElectroChem* **2020**, *7*, 4679–4684. [[CrossRef](#)]
95. Kolen, M.; Antoniadis, G.; Schreuders, H.; Boshuizen, B.; van Noordenne, D.D.; Ripepi, D.; Smith, W.A.; Mulder, F.M. Combinatorial Screening of Bimetallic Electrocatalysts for Nitrogen Reduction to Ammonia Using a High-Throughput Gas Diffusion Electrode Cell Design. *J. Electrochem. Soc.* **2022**, *169*, 124506. [[CrossRef](#)]
96. Kolen, M.; Ripepi, D.; Smith, W.A.; Burdyny, T.; Mulder, F.M. Overcoming Nitrogen Reduction to Ammonia Detection Challenges: The Case for Leapfrogging to Gas Diffusion Electrode Platforms. *ACS Catal.* **2022**, *12*, 5726–5735. [[CrossRef](#)] [[PubMed](#)]

**Disclaimer/Publisher's Note:** The statements, opinions and data contained in all publications are solely those of the individual author(s) and contributor(s) and not of MDPI and/or the editor(s). MDPI and/or the editor(s) disclaim responsibility for any injury to people or property resulting from any ideas, methods, instructions or products referred to in the content.